Science Advances
AAAS

Manuscript Template

FRONT MATTER

Title

- High-performance Wearable Thermoelectric Generator with Self-healing, Recycling and Lego-like Reconfiguring Capabilities

Teaser: Self-healable, recyclable, and Lego-like reconfigurable thermoelectric generator for wearable energy harvesting.

Authors

Wei Ren[1,2]†, Yan Sun[2,3,4]†, Dongliang Zhao[5,6]†, Ablimit Aili[2], Shun Zhang[2,7], Chuanqian Shi[2,8], Jialun Zhang[1], Huiyuan Geng[1], Jie Zhang[3,4], Lixia Zhang[1]*, Jianliang Xiao[2]*, Ronggui Yang[9,10]*

Affiliations

[1]State Key Laboratory of Advanced Welding and Joining, Harbin Institute of Technology, Harbin 150001, China.

[2]Department of Mechanical Engineering, University of Colorado Boulder, Boulder, CO 80309, USA.

[3]School of Materials Science and Engineering, Harbin Institute of Technology, Harbin 150001, China.

[4]Center of Analysis and Measurement, Harbin Institute of Technology, Harbin 150001, China.

[5]School of Energy and Environment, Southeast University, Nanjing 210096, China.

[6]Engineering Research Center of Building Equipment, Energy, and Environment, Ministry of Education, Southeast University, Nanjing 210096, China.

[7]Department of Engineering Mechanics, Soft Matter Research Center, and Key Laboratory of Soft Machines and Smart Devices of Zhejiang Province, Zhejiang University, Hangzhou 310027, China.

[8]School of Aerospace Engineering and Applied Mechanics, Tongji University, Shanghai 200092, China.

[9]School of Energy and Power Engineering, Huazhong University of Science and Technology, Wuhan 430074, China.

[10]State Key Laboratory of Coal Combustion, Huazhong University of Science and Technology, Wuhan 430074, China.

†These authors contributed equally to this work.

*Corresponding authors: ronggui.yang@hust.edu.cn (R.Y.); jianliang.xiao@colorado.edu (J.X.); zhanglxia@hit.edu.cn (L.Z.)

Abstract

Thermoelectric generators (TEGs) are an excellent candidate for powering wearable electronics and the 'Internet of Things', due to their capability of directly converting heat to electrical energy. Here we report a high-performance wearable TEG with superior stretchability, self-healability, recyclability and Lego-like reconfigurability, by combining modular thermoelectric chips, dynamic covalent polyimine, flowable liquid metal electrical wiring in a novel mechanical architecture design of "soft motherboard-rigid plugin modules". A record-high open-circuit voltage among flexible TEGs is achieved, reaching 1 V/cm^2 at temperature difference 95 K. Furthermore, this TEG is integrated with a wavelength-selective metamaterial film on the cold side, leading to greatly improved device performance under solar irradiation, which is critically important for wearable energy harvesting during outdoor activities. The unique properties and design concepts of TEGs reported here can pave the way for delivering the next-generation high-performance, adaptable, customizable, durable, economical and eco-friendly energy harvesting devices with wide applications.

MAIN TEXT

Introduction

Thermoelectric generators (TEGs) can directly convert low-grade heat to electricity, and thus are very promising energy sources for wearable electronics and 'Internet of Things' (*1*). However, conventional TEGs are rigid and brittle (*2–6*), and thus are not adaptable to the complex geometrical and compliant material properties of the human body. Recently, developing flexible TEG systems has attracted a lot of attention, including using thermoelectric (TE) films (*7*, *8*), TE bulks (*9*, *10*), printable TE inks (*11–15*), TE fibers (*16*, *17*) and organic TE materials (*18*, *19*). However, very few studies reported TEGs with good stretchability (*7*, *17*), which is critical to ensure conformal contact with complex geometries of human body for optimal thermoelectric performance (*20–28*). Inspired by the self-healing capability of human skin, self-healable electronics has also shown promising potential in wearable electronics for improved reliability and durability (*29–34*). However, this capability has not been achieved in TEG systems yet.

In this work, we report the first self-healable and recyclable TEG system with superior stretchability and thermoelectric performance. A record-high open-circuit voltage among flexible TEGs is achieved, reaching 1 V/cm^2 at temperature difference 95 K. Furthermore, this TEG system has the Lego-like reconfigurability, allowing users to customize the energy harvesting device according to thermal and mechanical conditions. These properties are realized by integrating high-performance modular thermoelectric chips, dynamic covalent thermoset polyimine as substrate and encapsulation, and flowable liquid metal as electrical wiring through a novel mechanical architecture design of "soft motherboard-rigid plugin modules". Finally, a wavelength-selective metamaterial film is introduced to the cold side of the TEG to enhance the thermoelectric performance under solar irradiation, which is critically important for wearable energy harvesting during outdoor activities.

Results

Device design and fabrication

The TEG is composed of modular thermoelectric chips, liquid metal as electrical wiring and dynamic covalent thermoset polyimine as both the substrate and encapsulation for liquid metal wiring (Fig. 1A). Polyimine can be synthesized by crosslinking three commercially available compounds, terephthalaldehyde, 3,3′-Diamino-*N*-

methyldipropylamine and tris(2-aminoethyl)amine (Supplementary Fig. S1) (*29*, *35*, *36*). To fabricate the thermoelectric chips, thin film Bi and Sb chalcogenides were deposited onto polyimide films using a thermal evaporator, serving as the *n*-legs and *p*-legs, respectively (Supplementary Fig. S2). The sizes of *n*-legs and *p*-legs were determined by a power conversion efficiency optimization process (Supplementary Note S1 and Table S1). To improve crystallinity and performance, the thermoelectric films were then treated at 320 °C for 26 min in argon atmosphere. Then Au-Ge electrodes were deposited using a thermal evaporator to form connections between *n*-legs and *p*-legs, which finishes the fabrication of thermoelectric chips (Supplementary Figs. S2 and S3A). The process of assembling modular thermoelectric chips into TEGs is schematically described in Fig. 1A. It started with laser cutting a polyimine substrate to create slots (Supplementary Fig. S3B), followed by screen printing patterned liquid metal electrical wirings (Supplementary Figs. S3C and S4). Then the modular thermoelectric chips were inserted into the slots of the polyimine substrate, and a small amount of the polyimine solution (terephthalaldehyde + 3,3′-Diamino-*N*-methyldipropylamine + tris(2-aminoethyl)amine in methanol) was applied to bond the thermoelectric chips with the substrate and to encapsulate the liquid metal wiring. The inset of Fig. 1A presents an exploded view of the device design, and Fig. 1B shows an optical image of the assembled TEG device. Detailed fabrication processes can be found in Supplementary Materials (Supplementary Note S2, Figs. S2 and S5).

Thanks to the bond exchange reactions within the dynamic covalent thermoset polyimine network and flowability of liquid metal electrical wiring (*29*, *36*), this TEG is self-healable, recyclable, and Lego-like reconfigurable, as schematically illustrated in Fig. 1A. Furthermore, this TEG has excellent mechanical properties. It can be bent (Fig. 1C), stretched (Fig. 1D), and worn on a finger (Fig. 1E) while functioning.

Power output and thermoelectric endurance

The power and voltage output of the TEG with 112 thermoelectric legs under various temperature differences were tested using a laboratory setup (Supplementary Fig. S6). Figures. 2A, 2B, and 2C exhibit the power generation (P_{out}) and open-circuit voltage (V_{oc}) per unit area at temperature differences (ΔT) ranging from 6 K to 95 K when the cold side temperature is fixed at 20 °C. The relation between power generation (P_{out}) and output voltage (V_{load}) at different temperature differences is given in Fig. 2A. Figure 2B shows that the max power generation P_{max} increases with temperature difference ΔT, and reaches 19 $\mu W/cm^2$ at ΔT = 93 K. The open-circuit voltage per unit area V_{oc}, as displayed in Fig. 2C, increases linearly with temperature difference, and reaches 1 V/cm^2 at ΔT = 95 K, which is remarkably higher than other flexible TEGs reported in literature (*7–19*). Figure 2D presents the endurance test results of this TEG. The power generation of the TEG remained stable for 100 hours when the hot side was fixed at 100 °C and the cold side was subject to indoor natural convection. The results indicate excellent thermal and electrical endurance of this TEG. Figure 2E shows a comparison with flexible TEGs reported in literature on six performance indexes, including max power density, max open-circuit voltage, flexibility (measured in bending radius), stretchability, self-healing and recyclability (*7–19*) (refer to Supplementary Table S2 and Fig. S7 for details). The TEGs reported here show flexibility and max power density comparable to other flexible TEGs, but the stretchability and max open-circuit voltage are much better. In addition, our TEGs are self-healable, recyclable, and Lego-like reconfigurable (to be demonstrated later), and these properties have not been demonstrated in TEG systems yet.

Wearable TEG and mechanical properties

This TEG has excellent mechanical flexibility and thus can be worn on human body for energy harvesting. Figure 3A shows a TEG attached on a forearm at room temperature 25 °C, and the inset gives the infrared measurement of temperature distribution across the device. Figure 3B shows that this TEG device can generate an average power output density of 45 nW/cm^2 and 83 nW/cm^2 and average output voltage of 25 mV/cm^2 and 33 mV/cm^2 when the wearer was sitting and walking, respectively (Supplementary Fig. S8). For the surface area of a typical sports wristband (6×25 cm^2), a power output of 12.5 μW and voltage output of 5 V can be generated when the wearer is walking, which is enough to directly drive most low-power sensor nodes with RF communication.

For wearable devices, the mechanical properties are of paramount importance. To improve the mechanical flexibility and stretchability of the TEG, an innovative design of "soft motherboard-rigid plugin modules" (SOM-RIP) is introduced. This design can effectively separate the rigid and fragile TEG chips from the strains in the soft polyimine substrate during mechanical deformation. Finite element method (FEM) simulation results, as shown in Figs. 3C and 3D, clearly prove the effectiveness of this SOM-RIP design on improving the mechanical properties of the TEG. Figure 3C exhibits the max principal strain distribution contour in the TEG when it's bent to a radius of 3.5 mm. The inset gives the maximum strain in the thermoelectric legs to be 0.0003%. Figure 3D shows the max principal strain distribution contour in the TEG when it's stretched by 120%. From the inset, the maximum strain in the thermoelectric legs is only 0.1%, which is below the fracture strain (≈ 0.15%) (*37*) of thermoelectric materials. This SOM-RIP design yields a strain reduction ratio of 1200 times. The strain distribution contours in polyimide and AuGe due to bending and stretching are given in Supplementary Fig. S9.

To ensure mechanical robustness, cyclic bending test was conducted, with a bending radius of 3.5 mm. As shown in Fig. 3E and Supplementary Fig. S10, the electrical resistance remains constant, and the power output doesn't show obvious variation. Figure 3F presents the relative resistance change and power output versus mechanical stretching strain. Both resistance and power output show no noticeable change when the TEG device is stretched by up to 120%. This is also demonstrated by the inset, as the brightness of the LED when it's stretched by 120% is comparable to that when the TEG is not stretched (Supplementary Fig. S11).

It's worth pointing out that the flexibility and stretchability of this TEG are limited along the direction parallel to the thermoelectric chips. However, TEGs with ultra-high flexibility and stretchability along one direction are well suited for cylindrical heat sources, such as arms, legs, and fingers for wearable applications, and industrial pipelines for waste heat harvesting.

Self-healing, recycling, and Lego-like reconfiguration

In this TEG, the flowability of liquid metal wiring and bond exchange reactions within the polyimine network provide excellent self-healing capability to the device (*29*). Figure 4A schematically illustrates the self-healing process and mechanism. After the liquid metal wiring and polyimine substrate are cut broken (top, Fig. 4A), the broken interfaces can be brought back in contact. The liquid metal wiring immediately regains electrical conductivity, due to its fluid like behavior. Bond exchange reactions promote generation of new covalent bonds at the interface, leading to healed TEG device with both mechanical robustness and electrical functionality (bottom, Fig. 4A). Figure 4B and

Supplementary Video S1 experimentally demonstrate this process using a TEG device with two thermoelectric modules. When the liquid metal wiring and polyimine substrate are cut broken, the LED turns off (top middle). Bringing the interfaces back to contact leads to immediate healing of the electrical conductivity in the liquid metal wiring, and the LED turns on again (bottom middle). After 1.5 hours healing at room temperature, sufficient covalent bonds are created at the interface, leading to a mechanically robust self-healed TEG that can be bent without affecting power output (right, Fig. 4B). Optical microscope images in Supplementary Fig. S12 exhibit the healing process of a cut in polyimine over time. The self-healed TEG demonstrates stretchability comparable to the original device, as it can be stretched by 120% without affecting the electrical resistance (Fig. 4C).

Excessive amine monomers can cause depolymerization of polyimine networks into monomers and oligomers soluble in organic solvents, leading to excellent recyclability of polyimine based devices (*29*). Figure 4D shows the recycling process of a TEG device. An old TEG is soaked in the recycling solution (3,3′-Diamino-*N*-methyldipropylamine and tris(2-aminoethyl)amine in methanol) (top left). After 6 hours at room temperature, the polyimine substrate completely depolymerizes into oligomers and monomers that are soluble in methanol (top right). Then the other components including thermoelectric modules, conductors and liquid metal can be separated from the chemical solution (bottom right). The recycled solution can be fully reused to synthesize a new polyimine film by proportionally adding terephthalaldehyde and methanol. A new functional TEG can be fabricated by using all components recycled from the old TEG (bottom left). As demonstrated in Fig. 4E, the power output of the new TEG is comparable to the old TEG.

Not only self-healable and recyclable, this TEG device is also Lego-like reconfigurable, thanks to the SOM-RIP construction that combines dynamic covalent thermoset polyimine and liquid metal wiring. Figure 4F demonstrates the reconfiguration of two separate TEG devices (device I and II) into a new TEG device (device III). The Lego-like reconfiguration process starts with cutting off one terminal of devices I and II to expose the liquid metal wiring (left, Fig. 4F), followed by bringing the exposed terminals of the two TEGs into physical contact. Then applying and curing a small amount of polyimine solution (terephthalaldehyde + 3,3′-Diamino-*N*-methyldipropylamine + tris(2-aminoethyl)amine in methanol) at the joint of the two TEGs completely heals the interface (middle, Fig. 4F). The new TEG is fully functional (right, Fig. 4F). This process is schematically illustrated in detail in Supplementary Fig. S13. As shown in Fig. 4G, the power output of the new TEG III is equal to the sum of I and II, indicating that the Lego-like reconfiguring process is effective without performance degradation. It's worth noting that during this reconfiguration process, it's not necessary to apply polyimine solution, but more time is required for generating enough covalent bonds at the joint interface. The Lego-like reconfiguration capability allows users to customize TEGs using modules in series or parallel for targeted form factors, constructions, output voltage and power based on specific thermal conditions and output of thermoelectric chips (Supplementary Fig. S14). The Lego-like reconfigurable TEG can also be integrated into a sensor system based on similar self-healing substrate to form a self-powered autonomous sensor system.

Enhancing outdoor performance of TEG with metamaterial film

The solar irradiance, ambient radiation, and non-radiative heat exchange can affect the wearable TEG performance during outdoor activities (top, Fig. 5A). The energy balance of the TEG's cold side that is exposed to the ambient can be expressed as (*38*):

$$Q_{surf} = P_{non-rad} + P_{rad} - P_{abs} = h_c\left(T_c - T_{amb}\right) + \kappa_B \overline{\varepsilon}_{emit}\left(T_c^4 - T_s^4\right) - P_{solar}\overline{\varepsilon}_{abs}, \quad (1)$$

where Q_{surf} is the total heat flow on the cold side surface per unit area, $P_{non\text{-}rad}$ and P_{rad} are the nonradiative heat transfer and thermal radiation exchange per unit area between the cold side surface and the ambient, respectively, P_{abs} is the absorbed solar irradiation power per unit area, P_{solar} is the solar irradiation power per unit area, and $\overline{\varepsilon}_{emit}$ and $\overline{\varepsilon}_{abs}$ are the effective emissivity and effective absorptivity of the surface, respectively. The emissivity and absorptivity can be used to evaluate the thermal radiation of the cold side surface and its absorption of the solar irradiation, as shown in Eq. (1). Fig. 5B shows the measured wavelength-dependent emissivity/absorptivity of the TEG surface (bare surface). The bare TEG surface has strong absorption (>0.87) in the solar spectra (0.3~2.5 μm), indicating that the surface can be heated up by solar irradiance which significantly restricts its heat dissipation. To enhance the outdoor TEG performance, the key is to modify the cold side surface to be wavelength-selective for more efficient heat dissipation. Such surface must possess two characteristics: 1) low absorptivity in the solar spectra, and 2) high emissivity in the infrared range, especially in the atmospheric transmission window (8~13 μm), which allows the cold side to emit infrared radiation to the universe through the atmosphere, namely radiative sky cooling (*38–40*). Therefore, a glass-polymer hybrid metamaterial film that can provide both characteristics is chosen and applied as a cover on the cold side surface of the TEG (bottom, Fig. 5A), which yields an efficient wavelength-selective surface. As shown in Fig. 5B, the measured wavelength-dependent emissivity/absorptivity of the wavelength-selective surface clearly shows much lower absorption than the bare surface in the solar spectra (0.3~2.5 μm), and comparable emissivity in the atmospheric transmission window (8~13 μm). The detailed design and fabrication of the metamaterial can be found in our previous work (*40*).

To quantitatively explore the effects of solar irradiance and radiative cooling on thermoelectric performance, TEGs were tested outdoors with both bare surface and wavelength-selective surface at the cold side on a sunny day using a laboratory setup (Supplementary Fig. S15). The measured solar irradiance, outdoor temperature and wind speed from 13:00 to 18:00 are presented in Fig. 5C. The sudden drop of the measured solar irradiance at 15:18 is because the weather station was shadowed by an adjacent building, and the TEG devices were shadowed by the building at 15:45. The heat exchange on the two types of surfaces can be calculated based on the measured data (Supplementary Note S3 and Fig. S16). As shown in Fig. 5D, the TEG with bare surface at the cold side has negative heat exchange between 13:00 and 15:45, because the solar absorption on the bare surface is more than the total heat dissipation by radiative and non-radiative heat transfer. This leads to the output voltage of the TEG with bare surface fluctuating around zero (Fig. 5E), and the power generation around only 1 nW/cm^2 (Fig. 5F) before 15:45. For the TEG with wavelength-selective surface at the cold side, the heat exchange remains stable both before and after the TEG was shadowed by the building, as shown in Fig. 5D. This leads to greatly improved TEG performance with output voltage ~ 40 mV/cm^2 (Fig. 5E) and output power ~ 10 nW/ cm^2 (Fig. 5F) before 15:45, when compared with the TEG with bare surface at the cold side. After the TEG devices were shadowed by a building at 15:45, the two TEGs with bare surface and wavelength-selective surface at the cold side have similar total heat exchange and thermoelectric performance, owing to their similar high emissivity in the atmospheric transmission window and the absence of solar irradiation.

Discussion

A high-performance wearable thermoelectric generator with superior stretching, self-healing, recycling, and Lego-like reconfiguration capabilities is reported in this work. To achieve these properties, high-performance modular thermoelectric chips, dynamic covalent thermoset polyimine as substrate and encapsulation, and flowable liquid metal as electrical wiring are integrated through a novel mechanical architecture design of "soft motherboard-rigid plugin modules". This TEG can produce a record-high open-circuit voltage density of 1 V/cm^2 at temperature difference 95 K among flexible TEGs, which is promising for harvesting low-grade heat to power 'Internet of Things' and wearable electronics. These features enable TEGs to be adaptable to the rapidly changing mechanical and thermal conditions, and user requirements. Furthermore, a wavelength-selective metamaterial film is integrated at the cold side of the TEG to simultaneously maximize the radiative cooling and minimize the absorption of solar irradiation. Therefore the thermoelectric performance can be greatly enhanced under solar irradiation, which is critically important for wearable energy harvesting during outdoor activities. The design concepts, approaches and properties of the TEG system reported in this work can pave the way for delivering the next-generation high-performance, adaptable, customizable, durable, economical and eco-friendly energy harvesting devices with wide applications.

It's also worth noting that the overall design concept of this work is scalable and adaptable to other thermoelectric materials and fabrication methods, including roll-to-roll physical vapor deposition and printing techniques (*41*). It's possible to further enhance the thermoelectric performance of the wearable TEG, by improving fabrication process of thermoelectric films, adopting thermoelectric films with better thermoelectric properties (*42–45*), and using traditional thermoelectric legs with much smaller dimensions.

Materials and Methods

Material synthesis and device fabrication

Thin-film thermoelectric materials were deposited on a polyimide film (125 μm, DuPont) by a thermal evaporator. The target materials of *p*-type legs and *n*-type legs for the evaporation were $Bi_{0.5}Sb_{1.5}Te_3$ and $Bi_2Te_{2.8}Se_{0.3}$ bulks, respectively, which were prepared by smelting Bi ingot (99.999%, Alfa Aesar), Sb ingot (99.999%, Alfa Aesar), Te ingot (99.999%, Alfa Aesar) and Se ingot (99.999%, Alfa Aesar) in sealed quartz tubes under vacuum below 10^{-3} Pa using a muffle furnace (KSL-1100X-L) at 1073 K for 5 hours. The deposited thermoelectric films were then heated at 320 °C for 26 min in Argon atmosphere using a tube furnace (OTF-1200X). Au-Ge thin-film electrodes were deposited by a thermal evaporator using Au88Ge12 alloy (99.99%, Kurt. J. Lesker) as the target material. The polyimine substrate is polymerized using three commercial compounds, terephthalaldehyde, 3,3′-Diamino-*N*-methyldipropylamine and tris(2-aminoethyl)amine. A mixture of 3,3′-Diamino-*N*-methyldipropylamine (1.251 g, 8.61 mmol) and tris(2-aminoethyl)amine (0.252 g, 1.72 mmol) was added to a 25 mL centrifuge tube with a screw cap followed by addition of methanol (20 mL) and terephthalaldehyde (1.5 g, 11.18 mmol). The mixture was stirred till the solution became translucent and yellow in color, then the solution was poured into petri dish coated with PDMS. The solution was cured by evaporative drying in a fume hood for at least 72 hours at room temperature. The recycling solution is a mixture of 3,3′-Diamino-*N*-methyldipropylamine (1.251 g, 8.61 mmol) and tris(2-aminoethyl)amine (0.252 g, 1.72 mmol) in methanol. The liquid metal (a mixture of 75.5% gallium and 24.5% indium by weight) was blended with 0.35 wt.% SiO_2 particles (radius 40 μm) to improve screen printing yield. The melting point of the liquid metal is 15.3 °C. Alternatively, eutectic gallium-indium-tin (Galinstan) (68% Ga, 22% In, and 10% Sn by weight) with a melting

point of -19 °C can be adopted for a colder environment. A laser cutting device (EPILOG 36EXT-MODEL9000) was used to prepare all the masks and slots in polyimine substrates. The wavelength-selective film was attached on the cold side of the TEG by using a pressure-sensitive tape.

Materials characterization.

The thicknesses of the thermoelectric films and Au-Ge film was measured by a stylus profiler (Bruker DektakXT). The surface microtopography and composition were analyzed using scanning electronic microscope (SEM) (Quanta 200FEG and Hitachi SU3500) accompanied by the energy dispersive X-ray spectroscopy (EDS). The Seebeck coefficient and electrical resistivity were measured by the four probe method on a simultaneous measurement system (ULVAC ZEM-3), and the thermal conductivity of the thermoelectric films (Supplementary Fig. S17) was measured by the time-domain thermoreflectance method (*46*) on a homemade system (Supplementary Table S1, Figs. S18 and S19). Optical microscope images of the self-healing process were obtained using a super depth of field digital microscope (KEYENCE VHX-1000E).

TEG output measurement

The indoor and outdoor performance of TEG were tested by homemade setups (Supplementary Figs. S6 and S15). The hot side is a temperature-controlled heating table. The cold side is a double-stage cooler (hydrocooling and Peltier cooler) which can accurately control the cold side temperature of TEG from 0 °C to room temperature. Type T thermocouples (wire diameter 0.127 mm, OMEGA TT-T-36) were used to test the cold and hot side temperatures of TEG. The thermocouple wires were fixed by holders beside the tested positions, and only the bare tips of the thermocouples closely touched the tested positions by the elasticity of the thermocouple wires to avoid extra heat loss. No grease, glue, tape, or clamp was used to fix the thermocouples. Room temperature was measured by a type T thermocouple placed in air near the TEG. All the data including the temperature, voltage and resistance were collected by a multifunctional data collector (Keysight 34970A). Infrared images were obtained by an infrared camera (FLIR T630sc). Solar irradiance, outdoor temperature and wind speed were tested by a weather station near the TEG.

Mechanical characterization

The stretch tests were carried on a homemade stretching equipment. Simulated strain distribution contours in the TEG were obtained using a commercial software Abaqus. The AuGe conductive layer was modeled as skin layer on the surface of the polyimide film and thermoelectric legs, and then meshed by four-node shell elements. The polyimide film, *p*-type and *n*-type thermoelectric legs, and polyimine substrate were modeled using eight-node solid elements. The elastic moduli of the AuGe, *n*-type legs, *p*-type legs, polyimide films and polyimine substrate were 69.2 GPa, 52 GPa, 46 GPa, 2.5 GPa and 2 MPa, respectively. The Poisson's ratio for them were 0.32, 0.25, 0.25, 0.34 and 0.35, respectively. A strain of 120% and bending radius of 3.5mm were separately applied to the model to simulate experimental conditions.

References and Notes

1. D. M. Rowe, *Modules, systems, and applications in thermoelectrics*. (CRC Press, 2012).
2. D. Kraemer, Q. Jie, K. McEnaney, F. Cao, W. Liu, L. A. Weinstein, J. Loomis, Z. Ren, G. Chen, Concentrating solar thermoelectric generators with a peak efficiency of 7.4%. *Nat. Energy*. **1**, 16153 (2016).

3. D. Kraemer, B. Poudel, H.-P. Feng, J. C. Caylor, B. Yu, X. Yan, Y. Ma, X. Wang, D. Wang, A. Muto, K. McEnaney, M. Chiesa, Z. Ren, G. Chen, High-performance flat-panel solar thermoelectric generators with high thermal concentration. *Nat. Mater.* **10**, 532–538 (2011).

4. F. Kim, B. Kwon, Y. Eom, J. E. Lee, S. Park, S. Jo, S. H. Park, B. S. Kim, H. J. Im, M. H. Lee, T. S. Min, K. T. Kim, H. G. Chae, W. P. King, J. S. Son, 3D printing of shape-conformable thermoelectric materials using all-inorganic Bi_2Te_3-based inks. *Nat. Energy*. **3**, 301–309 (2018).

5. M. Kishi, H. Nemoto, T. Hamao, M. Yamamoto, S. Sudou, M. Mandai, S. Yamamoto, Micro thermoelectric modules and their application to wristwatches as an energy source. *Eighteenth International Conference on Thermoelectrics. Proceedings, ICT'99 (Cat. No.99TH8407)*, Baltimore, MD, USA, 301-307 (1999).

6. M. T. Dunham, M. T. Barako, J. E. Cornett, Y. Gao, S. Haidar, N. Sun, M. Asheghi, B. Chen, K. E. Goodson, Experimental Characterization of Microfabricated Thermoelectric Energy Harvesters for Smart Sensor and Wearable Applications. *Adv. Mater. Technol.* **3**, 1700383 (2018).

7. K. Nan, S. Dongmin Kang, K. Li, K. Jun Yu, F. Zhu, J. Wang, A. C. Dunn, C. Zhou, Z. Xie, M. T. Agne, H. Wang, H. Luan, Y. Zhang, Y. Huang, G. Jeffrey Snyder, J. A. Rogers, Compliant and stretchable thermoelectric coils for energy harvesting in miniature flexible devices. *Sci. Adv.* **4**, eaau5849 (2018).

8. K. Itoigawa, H. Ueno, M. Shiozaki, T. Toriyama, S. Sugiyama, Fabrication of flexible thermopile generator. *J. Micromechanics Microengineering*. **15**, S233–S238 (2005).

9. S. Hong, Y. Gu, J. K. Seo, J. Wang, P. Liu, Y. Shirley Meng, S. Xu, R. Chen, Wearable thermoelectrics for personalized thermoregulation. *Sci. Adv.* **5**, eaaw0536 (2019).

10. T. Sugahara, Y. Ekubaru, N. Van Nong, N. Kagami, K. Ohata, L. T. Hung, M. Okajima, S. Nambu, K. Suganuma, Fabrication with Semiconductor Packaging Technologies and Characterization of a Large Scale Flexible Thermoelectric Module. *Adv. Mater. Technol.* **4**, 1800556 (2019).

11. S. J. Kim, J. H. We, B. J. Cho, A wearable thermoelectric generator fabricated on a glass fabric. *Energy Environ. Sci.* **7**, 1959–1965 (2014).

12. M. K. Kim, M. S. Kim, S. Lee, C. Kim, Y. J. Kim, Wearable thermoelectric generator for harvesting human body heat energy. *Smart Mater. Struct.* **23**, 105002 (2014).

13. S. E. Jo, M. K. Kim, M. S. Kim, Y. J. Kim, Flexible thermoelectric generator for human body heat energy harvesting. *Electron. Lett.* **48**, 1015–1017 (2012).

14. S. J. Kim, H. E. Lee, H. Choi, Y. Kim, J. H. We, J. S. Shin, K. J. Lee, B. J. Cho, High-Performance Flexible Thermoelectric Power Generator Using Laser Multiscanning Lift-Off Process. *ACS Nano*. **10**, 10851–10857 (2016).

15. K. Suemori, S. Hoshino, T. Kamata, Flexible and lightweight thermoelectric generators composed of carbon nanotube-polystyrene composites printed on film substrate. *Appl. Phys. Lett.* **103**, 153902 (2013).

16. J. Choi, Y. Jung, S. J. Yang, J. Y. Oh, J. Oh, K. Jo, J. G. Son, S. E. Moon, C. R. Park, H. Kim, Flexible and Robust Thermoelectric Generators Based on All-Carbon Nanotube Yarn without Metal Electrodes. *ACS Nano*. **11**, 7608–7614 (2017).

17. T. Sun, B. Zhou, Q. Zheng, L. Wang, W. Jiang, G. J. Snyder, Stretchable fabric generates electric power from woven thermoelectric fibers. *Nat. Commun.* **11**, 572 (2020).

18. C. Zheng, L. Xiang, W. Jin, H. Shen, W. Zhao, F. Zhang, C. Di, D. Zhu, A Flexible Self-Powered Sensing Element with Integrated Organic Thermoelectric Generator. *Adv. Mater. Technol.* **4**, 1900247 (2019).

19. K. Wan, P. J. Taroni, Z. Liu, Y. Liu, Y. Tu, G. Santagiuliana, I. C. Hsia, H. Zhang, O. Fenwick, S. Krause, M. Baxendale, B. C. Schroeder, E. Bilotti, Flexible and Stretchable Self-Powered Multi-Sensors Based on the N-Type Thermoelectric Response of Polyurethane/Na_x(Ni-ett)$_n$ Composites. *Adv. Electron. Mater.* **5**, 1900582 (2019).

20. J. A. Rogers, T. Someya, Y. Huang, Materials and mechanics for stretchable electronics. *Science* **327**, 1603–1607 (2010).

21. Y. M. Song, Y. Xie, V. Malyarchuk, J. Xiao, I. Jung, K. J. Choi, Z. Liu, H. Park, C. Lu, R. H. Kim, R. Li, K. B. Crozier, Y. Huang, J. A. Rogers, Digital cameras with designs inspired by the arthropod eye. *Nature* **497**, 95–99 (2013).

22. H. U. Chung, B. H. Kim, J. Y. Lee, J. Lee, Z. Xie, E. M. Ibler, K. H. Lee, A. Banks, J. Y. Jeong, J. Kim, C. Ogle, D. Grande, Y. Yu, H. Jang, P. Assem, D. Ryu, J. W. Kwak, M. Namkoong, J. Bin Park, Y. Lee, D. H. Kim, A. Ryu, J. Jeong, K. You, B. Ji, Z. Liu, Q. Huo, X. Feng, Y. Deng, Y. Xu, K. I. Jang, J. Kim, Y. Zhang, R. Ghaffari, C. M. Rand, M. Schau, A. Hamvas, D. E. Weese-Mayer, Y. Huang, S. M. Lee, C. H. Lee, N. R. Shanbhag, A. S. Paller, S. Xu, J. A. Rogers, Binodal, wireless epidermal electronic systems with in-sensor analytics for neonatal intensive care. *Science* **363**, eaau0780 (2019).

23. D. H. Kim, J. Viventi, J. J. Amsden, J. Xiao, L. Vigeland, Y. S. Kim, J. A. Blanco, B. Panilaitis, E. S. Frechette, D. Contreras, D. L. Kaplan, F. G. Omenetto, Y. Huang, K. C. Hwang, M. R. Zakin, B. Litt, J. A. Rogers, Dissolvable films of silk fibroin for ultrathin conformal bio-integrated electronics. *Nat. Mater.* **9**, 511–517 (2010).

24. Y. J. Hong, H. Jeong, K. W. Cho, N. Lu, D. H. Kim, Wearable and Implantable Devices for Cardiovascular Healthcare: from Monitoring to Therapy Based on Flexible and Stretchable Electronics. *Adv. Funct. Mater.* **29**, 1808247 (2019).

25. T. Sekitani, T. Yokota, U. Zschieschang, H. Klauk, S. Bauer, K. Takeuchi, M. Takamiya, T. Sakurai, T. Someya, Organic nonvolatile memory transistors for flexible sensor arrays. *Science* **326**, 1516–1519 (2009).

26. H. Jinno, K. Fukuda, X. Xu, S. Park, Y. Suzuki, M. Koizumi, T. Yokota, I. Osaka, K. Takimiya, T. Someya, Stretchable and waterproof elastomer-coated organic photovoltaics for washable electronic textile applications. *Nat. Energy*. **2**, 780–785 (2017).

27. M. Bariya, H. Y. Y. Nyein, A. Javey, Wearable sweat sensors. *Nat. Electron.* **1**, 160–171 (2018).

28. C. Wang, D. Hwang, Z. Yu, K. Takei, J. Park, T. Chen, B. Ma, A. Javey, User-interactive electronic skin for instantaneous pressure visualization. *Nat. Mater.* **12**, 899–904 (2013).

29. Z. Zou, C. Zhu, Y. Li, X. Lei, W. Zhang, J. Xiao, Rehealable, fully recyclable, and malleable electronic skin enabled by dynamic covalent thermoset nanocomposite. *Sci. Adv.* **4**, eaaq0508 (2018).

30. J. Kang, J. B. H. Tok, Z. Bao, Self-healing soft electronics. *Nat. Electron.* **2**, 144–150 (2019).

31. D. Son, J. Kang, O. Vardoulis, Y. Kim, N. Matsuhisa, J. Y. Oh, J. W. To, J. Mun, T. Katsumata, Y. Liu, A. F. McGuire, M. Krason, F. Molina-Lopez, J. Ham, U. Kraft, Y. Lee, Y. Yun, J. B. H. Tok, Z. Bao, An integrated self-healable electronic skin system fabricated via dynamic reconstruction of a nanostructured conducting network. *Nat. Nanotechnol.* **13**, 1057–1065 (2018).

32. B. C. Tee, C. Wang, R. Allen, Z. Bao, An electrically and mechanically self-healing composite with pressure- and flexion-sensitive properties for electronic skin applications. *Nat. Nanotechnol.* **7**, 825–832 (2012).

33. J. Kang, D. Son, G. J. N. Wang, Y. Liu, J. Lopez, Y. Kim, J. Y. Oh, T. Katsumata, J. Mun, Y. Lee, L. Jin, J. B. H. Tok, Z. Bao, Tough and Water-Insensitive Self-Healing Elastomer for Robust Electronic Skin. *Adv. Mater.* **30**, 1706846 (2018).

34. J. Y. Oh, D. Son, T. Katsumata, Y. Lee, Y. Kim, J. Lopez, H. C. Wu, J. Kang, J. Park, X. Gu, J. Mun, N. G. J. Wang, Y. Yin, W. Cai, Y. Yun, J. B. H. Tok, Z. Bao, Stretchable self-healable semiconducting polymer film for active-matrix strain-sensing array. *Sci. Adv.* **5**, eaav3097 (2019).

35. Y. Jin, Z. Lei, P. Taynton, S. Huang, W. Zhang, Malleable and Recyclable Thermosets: The Next Generation of Plastics. *Matter*. **1**, 1456–1493 (2019).

36. P. Taynton, K. Yu, R. K. Shoemaker, Y. Jin, H. J. Qi, W. Zhang, Heat- or water-driven malleability in a highly recyclable covalent network polymer. *Adv. Mater.* **26**, 3938–3942 (2014).

37. W. Liu, Q. Jie, H. S. Kim, Z. Ren, Current progress and future challenges in thermoelectric power generation: From materials to devices. *Acta Mater.* **87**, 357–376 (2015).

38. D. Zhao, A. Aili, Y. Zhai, S. Xu, G. Tan, X. Yin, R. Yang, Radiative sky cooling: Fundamental principles, materials, and applications. *Appl. Phys. Rev.* **6**, 021306 (2019).

39. D. Zhao, A. Aili, Y. Zhai, J. Lu, D. Kidd, G. Tan, X. Yin, R. Yang, Subambient Cooling of Water: Toward Real-World Applications of Daytime Radiative Cooling. *Joule* **3**, 111-123 (2019).

40. Y. Zhai, Y. Ma, S. N. David, D. Zhao, R. Lou, G. Tan, R. Yang, X. Yin, Scalable-manufactured randomized glass-polymer hybrid metamaterial for daytime radiative cooling. *Science* **355**, 1062–1066 (2017).

41. S. Jo, S. Choo, F. Kim, S. H. Heo, J. S. Son, Ink Processing for Thermoelectric Materials and Power-Generating Devices. *Adv. Mater.* **31**, 1804930 (2019).

42. Q. Jin, S. Jiang, Y. Zhao, D. Wang, J. Qiu, D.-M. Tang, J. Tan, D.-M. Sun, P.-X. Hou, X.-Q. Chen, K. Tai, N. Gao, C. Liu, H.-M. Cheng, X. Jiang, Flexible layer-structured Bi_2Te_3 thermoelectric on a carbon nanotube scaffold. *Nat. Mater.* **18**, 62–68 (2019).

43. R. Venkatasubramanian, E. Siivola, T. Colpitts, B. O'Quinn, Thin-film thermoelectric devices with high room-temperature figures of merit. *Nature*. **413**, 597–602 (2001).

44. L. M. Goncalves, C. Couto, J. H. Correia, P. Alpuim, G. Min, D. M. Rowe, Optimization of thermoelectric thin-films deposited by co-evaporation on plastic substrates. *4th Eur. Conf. Thermoelectr. Proc.*, 12 (2006).

45. A. Giani, A. Boulouz, F. Pascal-Delannoy, A. Foucaran, E. Charles, A. Boyer, Growth of Bi_2Te_3 and Sb_2Te_3 thin films by MOCVD. *Mater. Sci. Eng. B Solid-State Mater. Adv. Technol.* **64**, 19–24 (1999).

46. P. Jiang, X. Qian, R. Yang, Time-domain thermoreflectance (TDTR) measurements of anisotropic thermal conductivity using a variable spot size approach. *Rev. Sci. Instrum.* **88**, 074901 (2017).

Acknowledgments: Funding: The authors acknowledge financial support from National Science Foundation, USA (CMMI-1762324) and National Key R&D Program of China (2019YFA0705201). D.Z. acknowledges the support from Natural Science Foundation of Jiangsu Province, China (BK2020041466). **Author contributions:** W.R., Y.S., D.Z., L.Z., J.X., and R.Y. conceived and designed the experiment. W.R. and Y.S. fabricated TEGs and performed the mechanical test and indoor output test. W.R., Y.S., D.Z. and A.A. conducted the outdoor test of TEGs. W.R., Y.S. and J.Z. measured and characterized the thermoelectric films, modified liquid metal and polyimine. S.Z. performed FEM simulations. Y.S. and C.S. fabricated the polyimine. W.R., J.-L.Z., and H.G. designed and fabricated the thermoelectric material targets. W.R., Y.S., D.Z., A.A., L.Z., J.X. and R.Y. analyzed experimental data. W.R., Y.S., D.Z., L.Z., J.X., and R.Y. wrote the paper. All authors discussed the results and commented on the manuscript. **Competing interests:** The authors declare no competing interests. **Data and materials availability:** All data needed to evaluate the conclusions in the paper are present in the paper and/or the Supplementary Materials. Additional data related to this paper may be requested from the authors.

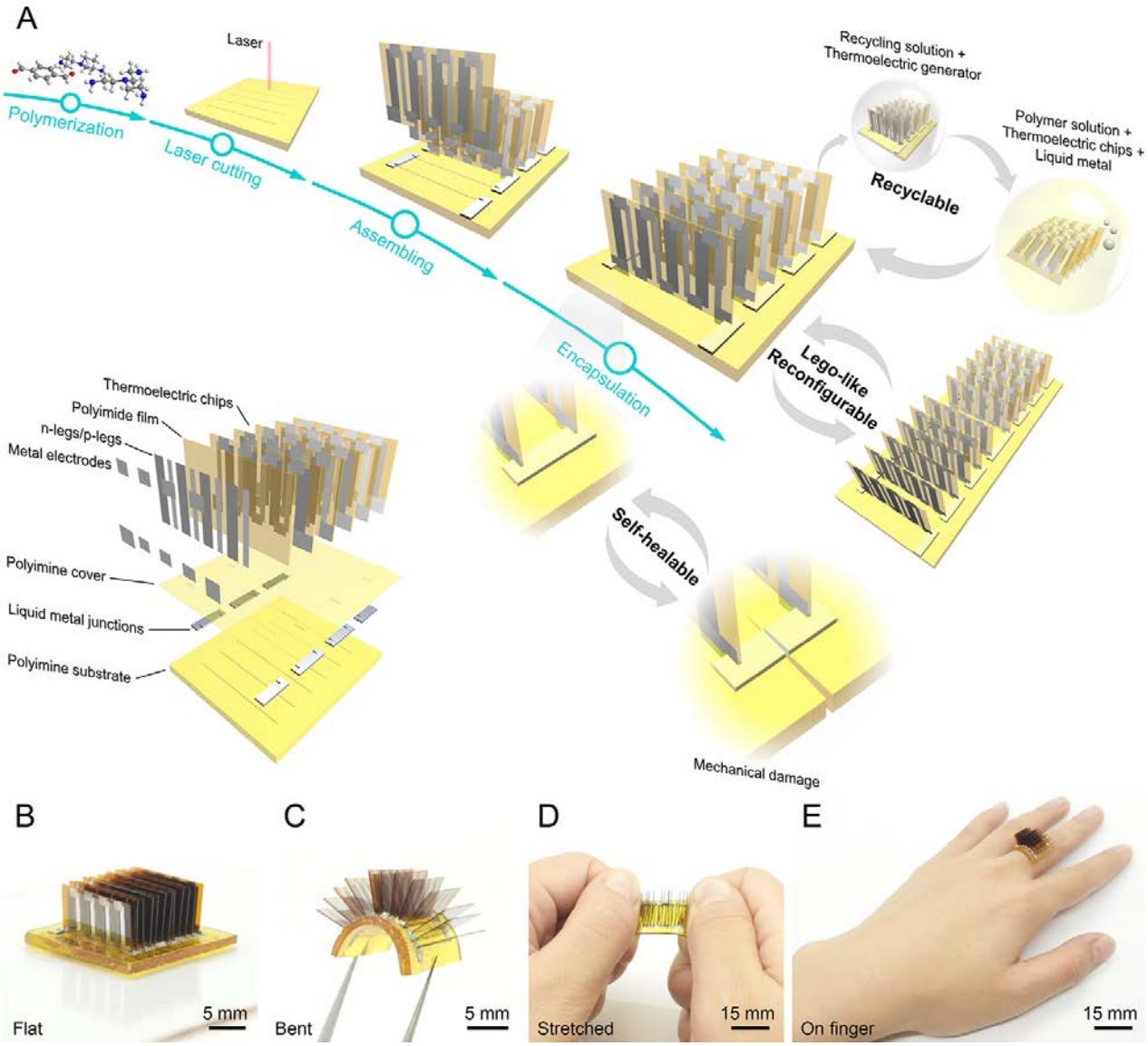

Fig. 1. Design and fabrication of the thermoelectric generator (TEG). (**A**), Schematic illustration of the design, fabrication process, and key characteristics, including self-healability, recyclability and Lego-like reconfigurability. Optical images of the TEG when it's flat (**B**), bent (**C**), stretched (**D**) and worn on the finger (**E**). Photo credit: Yan Sun, University of Colorado Boulder.

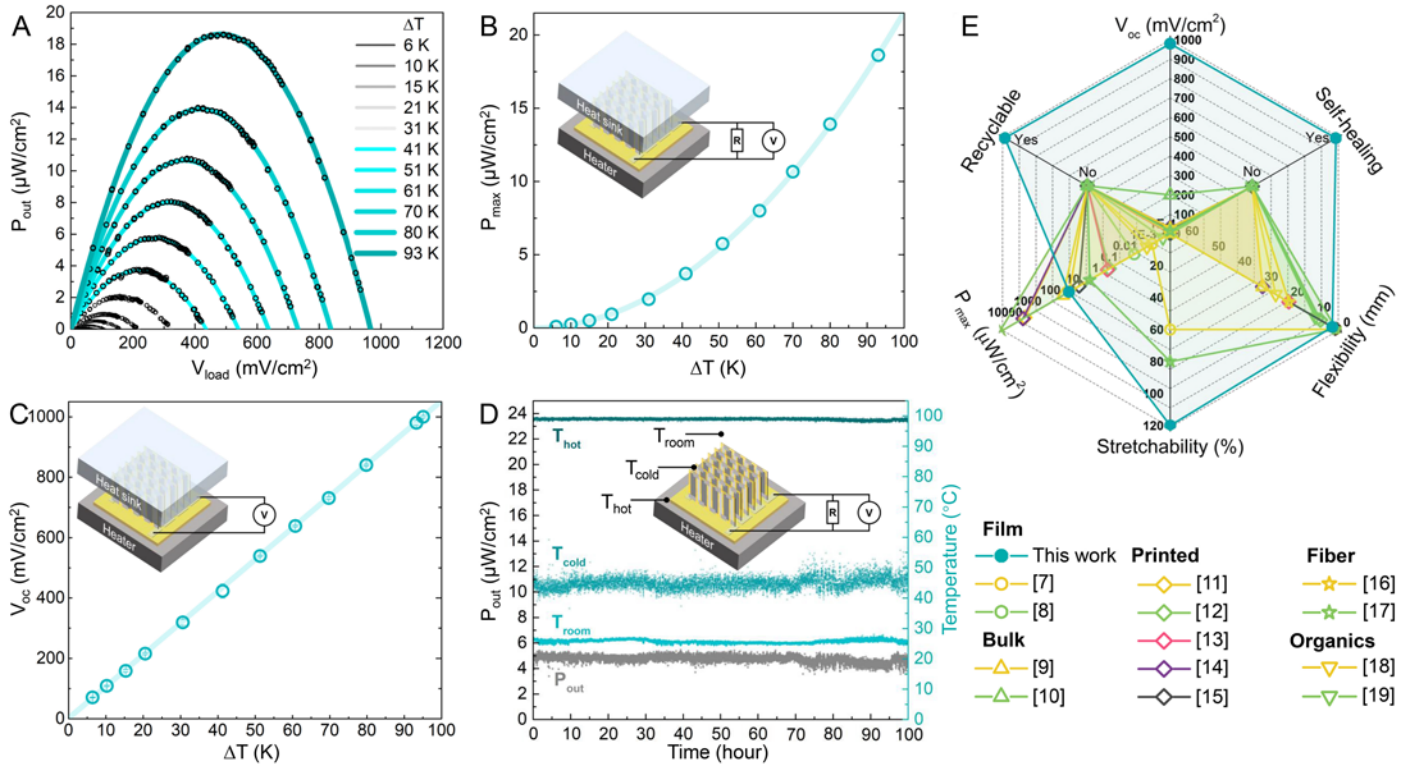

Fig. 2. Output and endurance of TEGs. (**A**), Power generation (P_{out}) as a function of output voltage (V_{load}) at various temperature differences (ΔT), with cold side temperature (T_{cold}) kept at 20 °C. The black points are measurement data. (**B**), Maximum power generation (P_{max}) versus temperature difference. (**C**), Open-circuit voltage (V_{oc}) versus temperature difference. The solid lines in (A) and (B) are fitting curves using parabolic functions. The solid line in (C) is a linear fitting curve. (**D**), 100-hour endurance test with the hot side temperature (T_{hot}) kept at 100 °C. The cold side was natural convection, and the room temperature (T_{room}) was around 26 °C. (**E**), Performance comparison between this TEG and other flexible TEGs reported in the literature (see supplementary materials for details). Flexibility refers to the minimum bending radius of TEGs experimentally demonstrated in the literature.

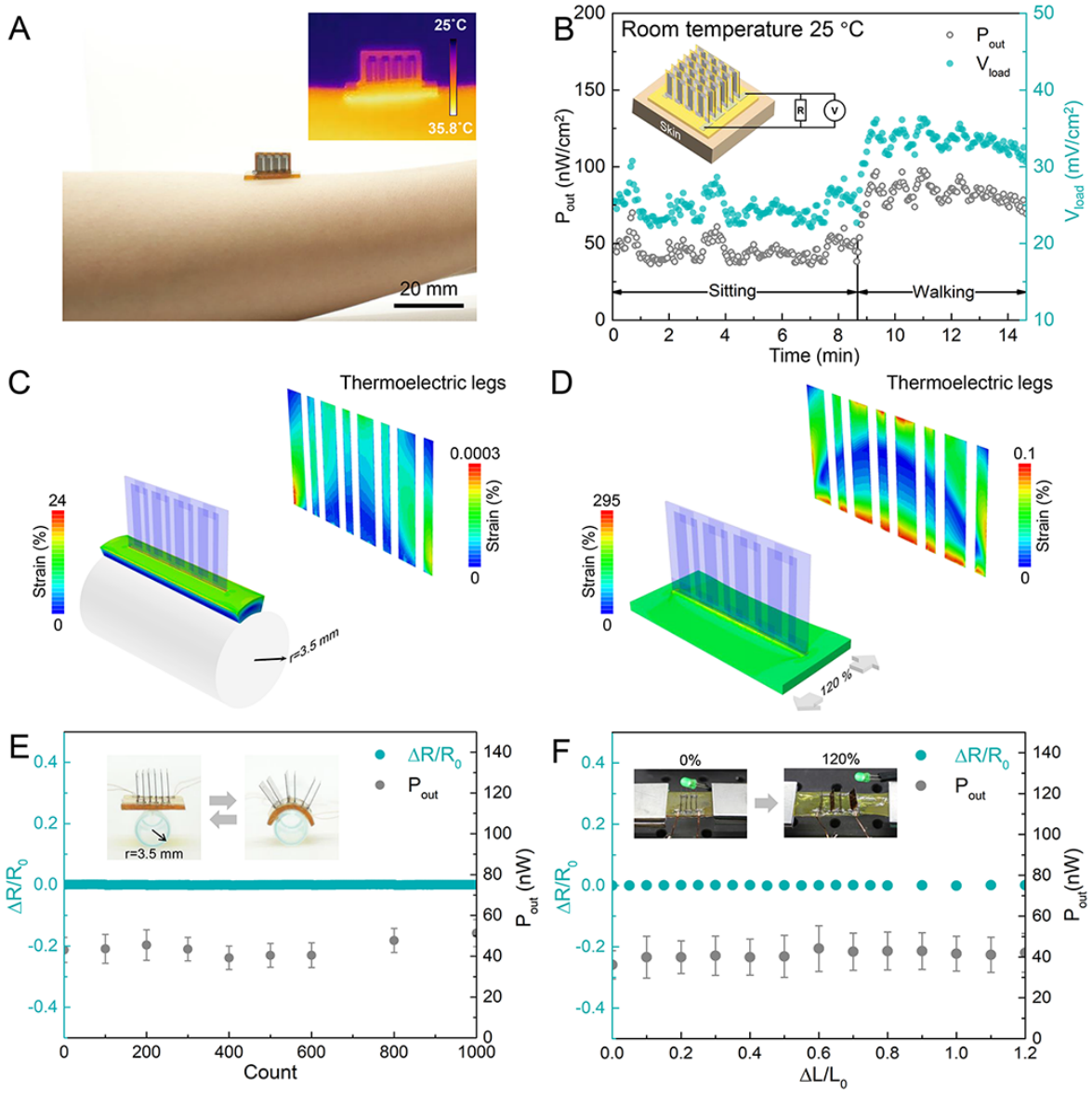

Fig. 3. Wearable energy harvesting and mechanical properties of the TEG. (**A**), Optical and infrared (inset) images of a TEG attached on an arm. (**B**), Power generation (P_{out}) and output voltage (V_{load}) of the TEG with 112 thermoelectric legs on the human skin when the wearer was sitting and walking. The cold side was natural convection. FEM simulated strain distribution contours in the TEG and thermoelectric legs (inset) when the TEG is bent to a radius of 3.5 mm (**C**) and stretched by 120% (**D**). (**E**), Relative electrical resistance change and power generation stability over 1000 bending cycles. The inset shows optical images of the TEG when it's flat and bent. The bending radius r = 3.5 mm, R_0 is the original resistance, and ΔR is the change in resistance. (**F**), Relative electrical resistance change and power generation versus stretching ratio ($\Delta L/L_0$). For output power (P_{out}) measurements in (E) and (F), the hot side temperature was kept at 41 °C, the cold side was natural convection, and the room temperature was around 26 °C. The inset in (F) shows optical images of a TEG during tension test, which is in series with a LED and a 4V DC source for visual demonstration (Supplementary Fig. S11) Photo credit: Yan Sun, University of Colorado Boulder.

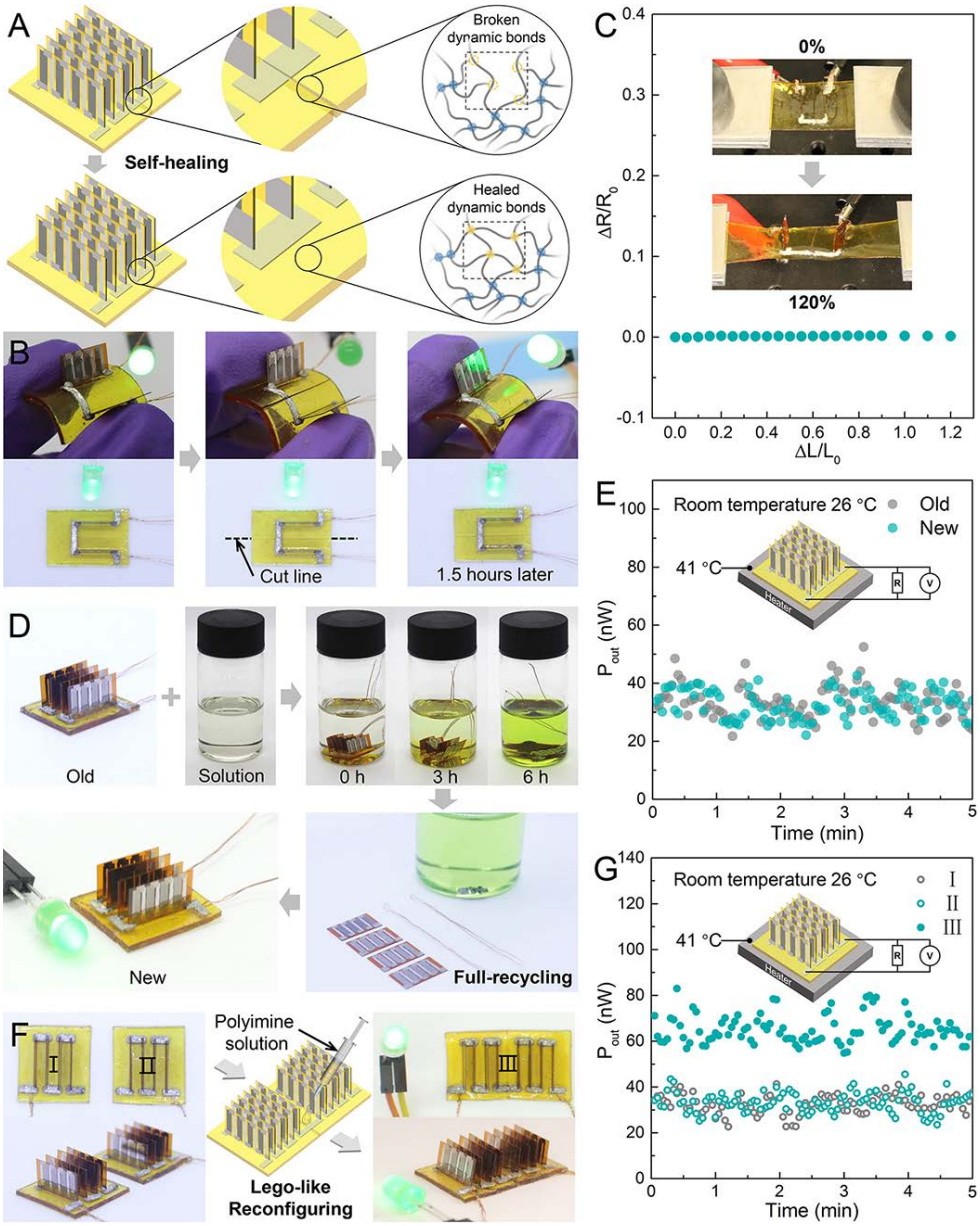

Fig. 4. Self-healing, recycling and Lego-like reconfiguration. (**A**), Schematic illustration of self-healing mechanism. (**B**), Optical images of the TEG in a self-healing test. The original TEG is flexible and in series with a LED and a 4V DC source (left). When the liquid metal electrical wiring and polyimine substrate are both cut broken, the LED turns off (top middle). When the two surfaces at the broken site are brought into contact, the liquid metal electrical wiring heals immediately, leading to the LED to turn on (bottom middle). After 1.5 hours, the polyimine substrate completely heals and regains mechanical robustness (right). (**C**), Relative electrical resistance change ($\Delta R/R_0$) of a self-healed TEG versus stretching ratio. The inset shows optical images of the self-healed TEG during tension test. (**D**), Optical images of the TEG at different recycling steps. The new TEG is in series with a LED and a 4V DC source (bottom left). (**E**), Power generation comparison between the old TEG and the recycled new TEG. (**F**), Lego-like reconfiguration of two separate TEGs (I and II) into a new functional TEG (III). The new TEG (III) is in series with a LED and a 4V DC source (right). (**G**), Power generation comparison between TEGs I, II and III. Photo credit: Yan Sun, University of Colorado Boulder.

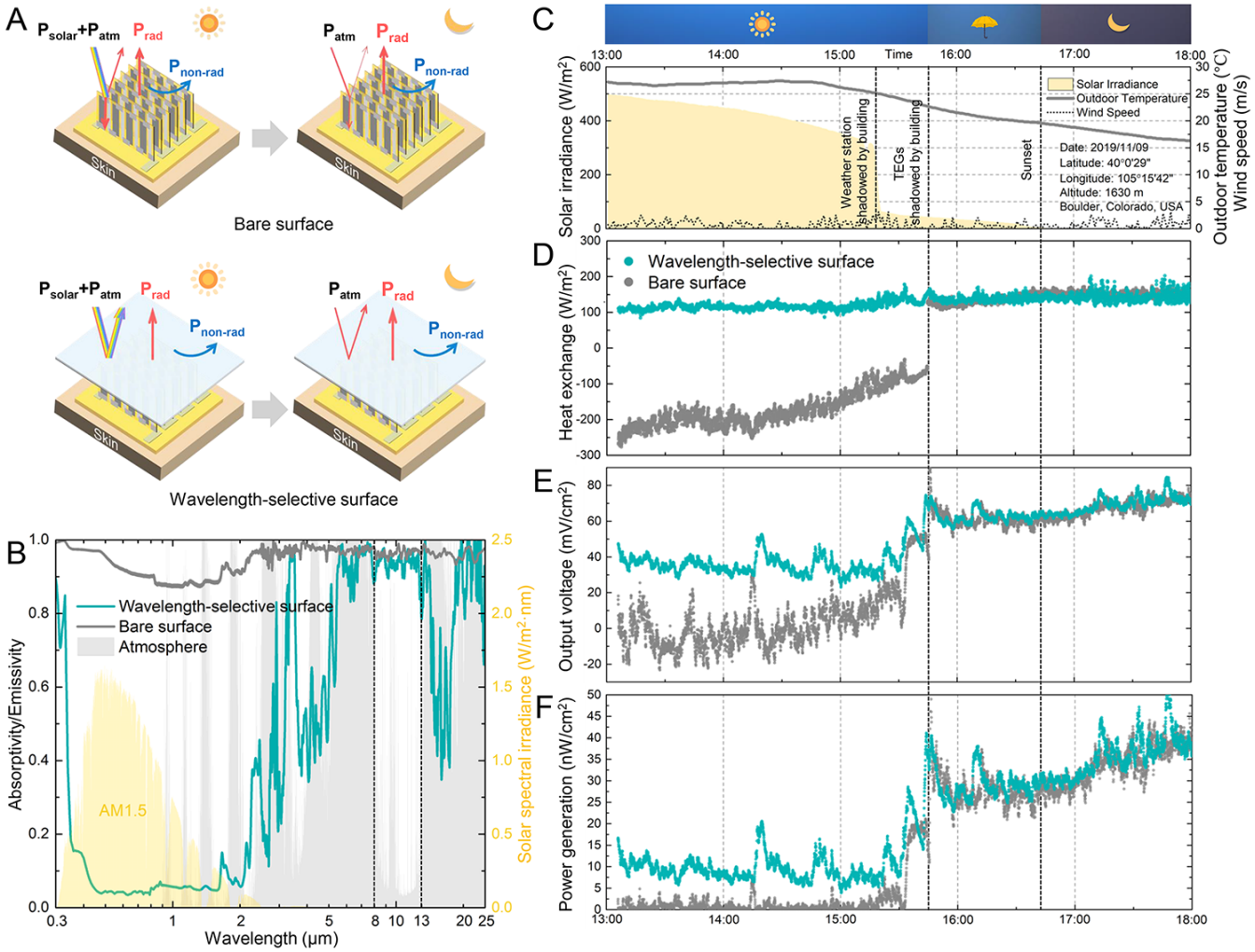

Fig. 5. Outdoor performance enhancement with wavelength-selective metamaterial films. (**A**), Schematic illustration of heat transfer processes of TEGs with bare surface (top) and wavelength-selective surface (bottom) during the daytime and nighttime. P_{solar} and P_{atm} are the solar irradiation power and atmospheric radiation power on the surface, respectively, P_{rad} is the thermal radiation power from the surface, and $P_{non\text{-}rad}$ is the non-radiative heat transfer (convection and conduction) between the surface and ambient. (**B**), Measured absorptivity/emissivity of the bare surface and wavelength-selective surface from 300 nm to 25 μm. The absorptivity/emissivity of the atmosphere (gray block) and power density of spectral solar irradiance (yellow block, air mass 1.5) are also included. Both the bare surface and wavelength-selective surface have strong emission between 8 and 13 μm (atmospheric transmission window), indicating excellent radiative cooling performance. The bare surface has strong absorption at full solar spectrum (> 0.87) and other infrared bands (> 0.96), while the wavelength-selective surface has much weaker absorption at solar spectrum than at infrared bands. (**C**), Solar irradiance, outdoor temperature and wind speed measured by a weather station from 13:00 to 18:00 (11/09/2019, Boulder, CO, USA). Total surface heat exchange (**D**), output voltage (**E**) and power generation (**F**) of the TEGs with bare surface and wavelength-selective surface at the cold side from 13:00 to 18:00.

Supplementary Materials

Note S1. Conversion efficiency optimization for thermoelectric generators.

Note S2. Fabrication processes of thermoelectric generators.

Note S3. Heat transfer model for bare surface and wavelength-selective surface.

Fig. S1. Polymerization of polyimine using three commercially available monomers.

Fig. S2. Schematic illustration of step-by-step fabrication processes of thermoelectric chips and polyimine substrates.

Fig. S3. Optical image of thermoelectric chips, a polyimine substrate with laser cutting slots, and printed liquid metal wirings on a polyimine substrate at room temperature.

Fig. S4. Scanning electron microscope (SEM) image and energy spectrum mapping of liquid metals mixed with SiO_2 microspheres.

Fig. S5. Schematic illustration of step-by-step fabrication processes of thermoelectric generators.

Fig. S6. Testing platform for the output of TEGs.

Fig. S7. Performance comparison between the TEG in this work and other flexible TEGs reported in the literature. Temperature difference dependent P_{max} and V_{oc}.

Fig. S8. Images of on-arm performance testing of a TEG during sitting and walking.

Fig. S9. Simulated strain distribution contours in the polyimide film, AuGe, and thermoelectric legs.

Fig. S10. Relative electrical resistance change and power generation stability over 1000 bending cycles with bending radius r =3.5 mm when the TEG is flat and bent.

Fig. S11. Schematic illustration of the circuit to visually exhibit that the TEG is undamaged when stretched, cut, recycled, or reconfigured.

Fig. S12. Optical microscope images and schematic illustration of the self-healing process at room temperature.

Fig. S13. Schematic illustration of step-by-step reconfiguration processes.

Fig. S14. Output performance of one thermoelectric chip.

Fig. S15. Outdoor performance testing setup for TEGs.

Fig. S16. Surface temperature, temperature difference, calculated radiative and nonradiative heat dissipation and heat absorption.

Fig. S17. SEM images of cross sections of *n*-type and *p*-type films.

Fig. S18. Schematics of physical properties test methods for thermoelectric films.

Fig. S19. Measured TDTR signal of *n*-type and *p*-type thermoelectric films.

Table S1. Physical properties of thermoelectric films at room temperature.

Table S2. A summary of experimental results of flexible TEGs reported in the literature, grouped by fabrication methods of thermoelectric materials.

Video S1. Self-healing process of the TEG.

Note S1. Conversion efficiency optimization for thermoelectric generators

Thermoelectric generators can directly convert heat into electricity. The conversion efficiency can be expressed as:

$$\eta = \frac{T_h - T_c}{T_h} \times \frac{\left(1+Z\overline{T}\right)^{\frac{1}{2}} - 1}{\left(1+Z\overline{T}\right)^{\frac{1}{2}} + \frac{T_h}{T_c}}, \tag{S1}$$

where T_h, T_c and $\overline{T}$ are the hot side temperature, cold side temperature, and average temperature of the hot side and cold side, respectively. Z can be expressed as:

$$Z = \frac{\left(\alpha_p - \alpha_n\right)^2}{\rho_n\kappa_n + \rho_p\kappa_p + \frac{L_n}{A_n}\frac{A_p}{L_p}\rho_n\kappa_p + \frac{L_p}{A_p}\frac{A_n}{L_n}\rho_p\kappa_n}, \tag{S2}$$

where ρ, κ, L, and A are the electrical resistivity, thermal conductivity, length of legs, and cross-sectional area of legs, respectively. The subscript n and p represent n-type and p-type legs, respectively.

The thermoelectric generator can be optimized to achieve the maximum conversion efficiency, η_{max}, when

$$\frac{L_n}{A_n}\frac{A_p}{L_p} = \left(\frac{\rho_p\kappa_n}{\rho_n\kappa_p}\right)^{\frac{1}{2}}, \tag{S3}$$

By substituting the data in Table S1 into formula (S3), it can be shown that when L_n=L_p and W_n/W_p = 0.498, the conversion efficiency of TEG in this work reaches the maximum value. Here W_n and W_p are the width of n-type and p-type legs, respectively.

Note S2. Fabrication processes for thermoelectric generators

Fabrication of thermoelectric chips

1) Prepare masks using laser cutting.

2) Clean the polyimide (PI) film with acetone.

3) Attach the *n*-type mask on top of the polyimide (PI) film.

4) Evaporate 1.6 μm *n*-type film in the vacuum using a thermal evaporator with a deposition rate of 1 nm/s.

5) Attach the *p*-type mask on top of the PI.

6) Evaporate 1.76 μm *p*-type film in the vacuum using a thermal evaporator with a deposition rate of 1 nm/s.

7) Heat the *n*-type and *p*-type films at 320 °C for 26 min in Argon atmosphere.

8) Attach the electrode mask on top of the PI.

9) Evaporate 200 nm Au-Ge electrodes in the vacuum using a thermal evaporator with a deposition rate of 0.5 nm/s.

Polymerization and laser cutting of polyimine substrates

1) A mixture of 3,3′-Diamino-*N*-methyldipropylamine (1.251 g, 8.61 mmol) and tris(2-aminoethyl)amine (0.252 g, 1.72 mmol) was added to a 25 mL centrifuge tube with a screw cap followed by addition of methanol (20 mL) and terephthalaldehyde (1.5 g, 11.18 mmol).

2) The mixture was stirred until the solution became translucent and yellow.

3) The polyimine solution was poured into a petri dish coated with PDMS.

4) The solution was cured by evaporative drying in a fume hood for at least 72 hours at room temperature.

5) The locating slots in the polyimine films (thickness 1 mm) were cut using a laser cutting equipment. The depth of the slots is 0.4 mm.

Printing liquid metal wiring

1) Mix liquid metal with 0.35 wt.% SiO_2 microspheres (radius 40 μm).

2) Attach the mask on top of the polyimine substrate.

3) Screenprint liquid metal electrical wires on top of the polyimine substrate. The thickness of liquid metal wiring was about 200 μm.

Assembling and encapsulation

1) Insert thermoelectric chips into the slots of the polyimine substrate.

2) Bond thermoelectric chips to the polyimine substrate, and encapsulate the liquid metal wiring using polyimine solution.

3) Wait for 0.5 hours to cure the polyimine. The thickness of the polyimine cover layer is about 50 μm.

Note S3. Heat transfer model for bare surface and wavelength-selective surface

The total heat exchange on the surface of a TEG can be expressed as:

$$Q_{surfi} = P_{non-rad} + P_{rad} - P_{abs}, \tag{S4}$$

where Q_{surfi} is the total heat transfer of the surface per unit area, P_{abs} is the absorbed solar power per unit area, P_{rad} is the thermal radiation power per unit area from the surface, and $P_{non-rad}$ is the nonradiative heat transfer (convection and conduction) per unit area between the surface and ambient.

The absorbed solar power per unit area is given by:

$$P_{abs} = \frac{1}{A}\cos\theta \int \varepsilon_s(\theta,\lambda) I_{solar}(\lambda) d\lambda, \tag{S5}$$

where θ is the angle between the incident direction of solar irradiation and the normal direction of the surface, $\varepsilon_s(\theta,\lambda)$ is the emissivity of the surface as a function of direction and wavelength, $I_{solar}(\lambda)$ is the direct spectral solar irradiance, and A is the total radiative cooling surface area.

The total radiative power per unit area (P_{rad}) from a surface is given by:

$$P_{rad} = \frac{1}{A}\int \cos\varphi d\varphi \int_0^\infty \varepsilon_s(\varphi,\lambda) I_{bb}(\lambda,T_c) d\lambda, \tag{S6}$$

where T_c is the surface temperature, φ is the solid angle between the direction of radiation and normal to the surface.

The nonradiative heat transfer per unit area can be expressed as

$$P_{non-rad} = \frac{1}{A} h_c (T_c - T_{amb}), \tag{S7}$$

where h_c is the overall heat transfer coefficient of nonradiative heat transfer between the TEG and ambient.

T_c and $\varepsilon_s(\theta,\lambda)$ are obtained from testing data (Fig. 5B and Supplementary Fig. S15). The calculated results are shown in Figs. 5C-F and Supplementary Fig. S15.

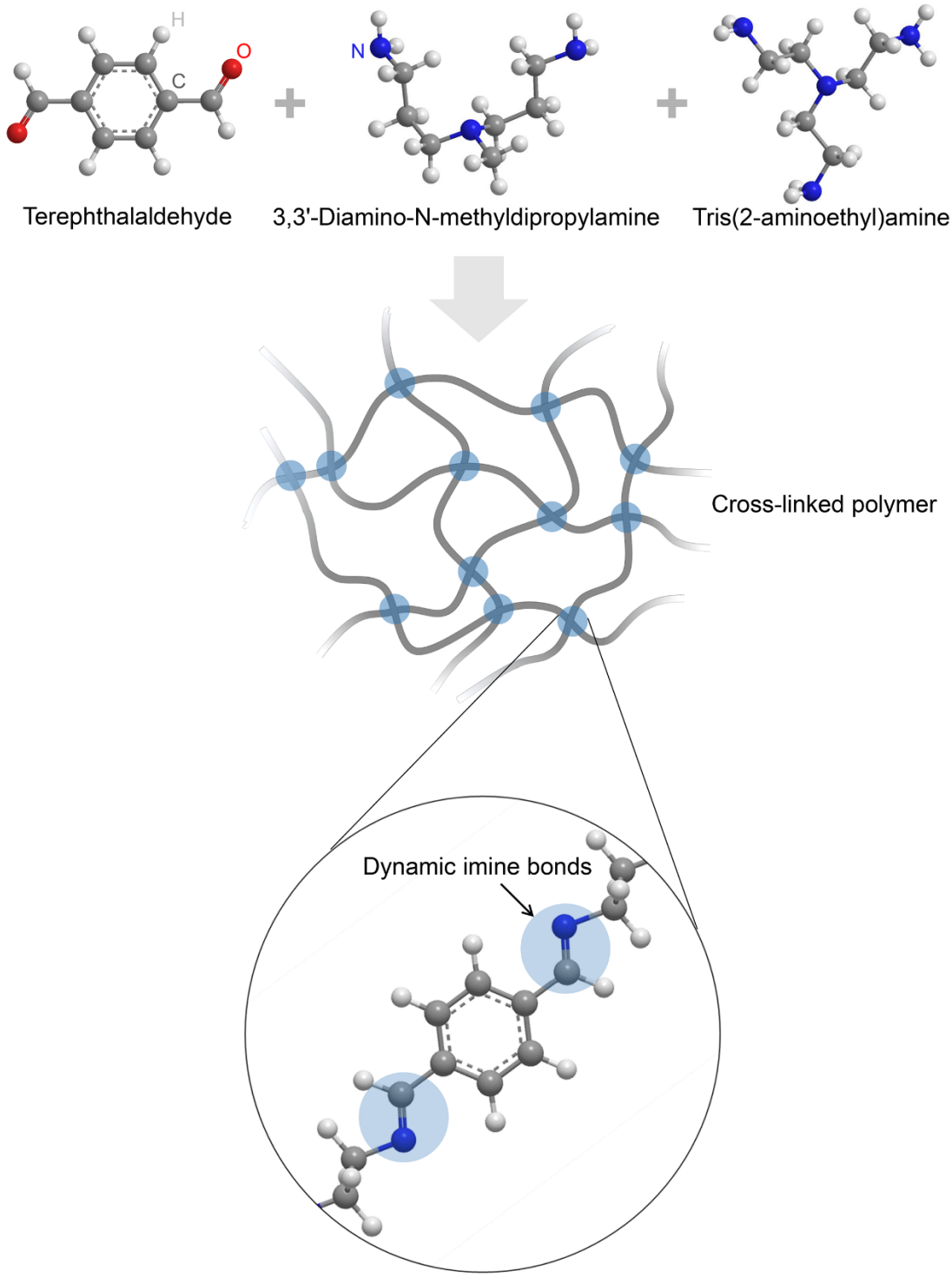

Fig. S1. Polymerization of polyimine using three commercially available monomers.

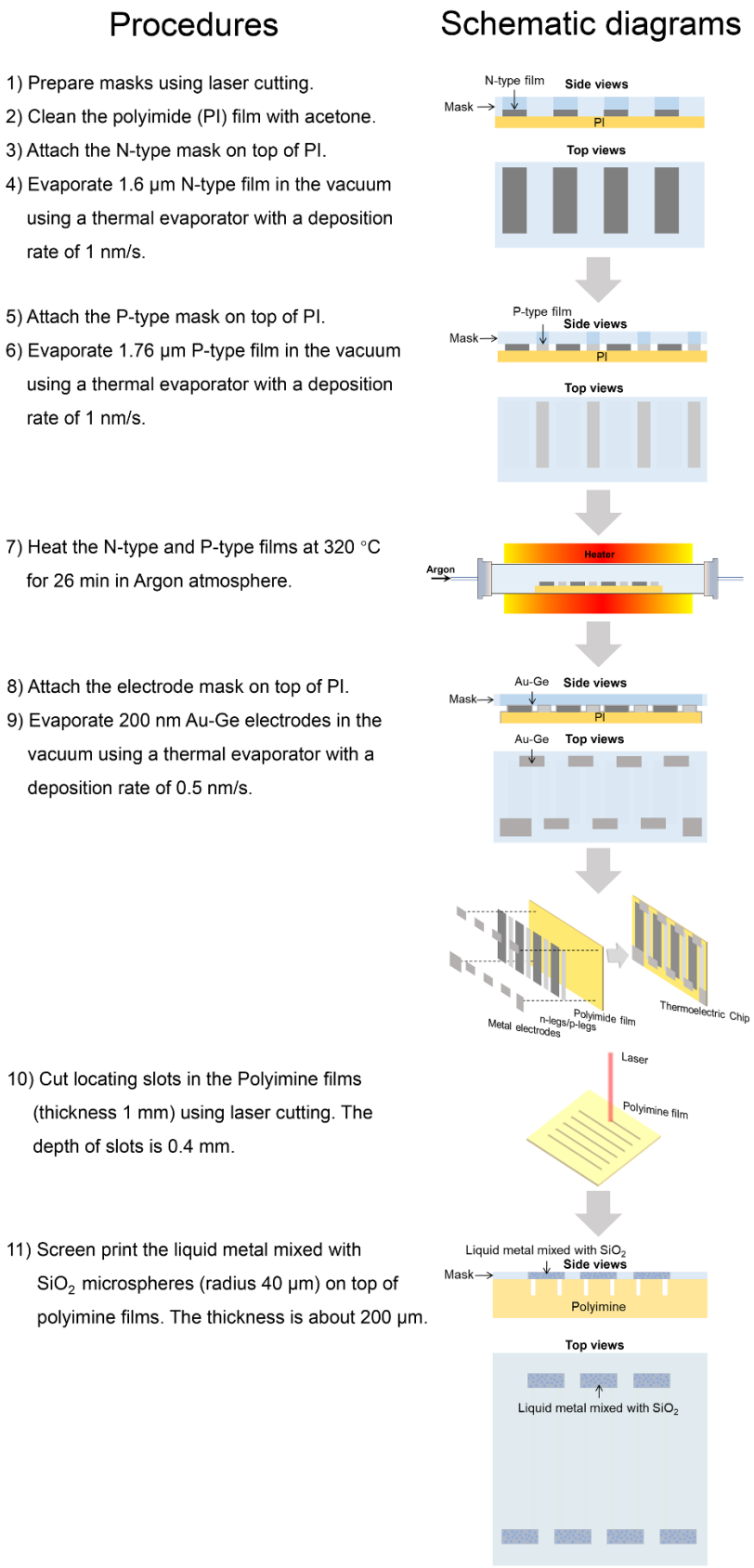

Fig. S2. Schematic illustration of step-by-step fabrication processes of thermoelectric chips and polyimine substrates.

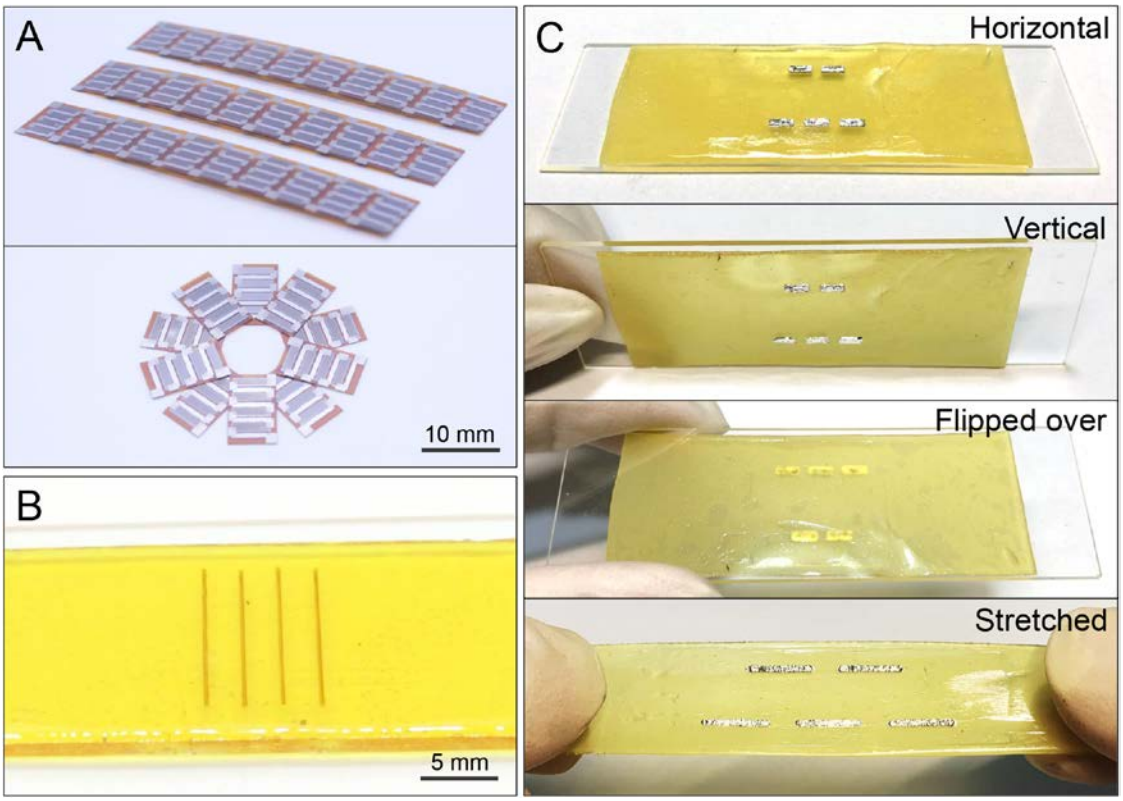

Fig. S3. (**A**) Optical image of thermoelectric chips. (**B**) Optical image of a polyimine substrate with laser cutting slots. (**C**) Optical image of the printed liquid metal wirings on a polyimine substrate at room temperature, when the substrate is horizontal, vertical, flipped over, and stretched. Photo credit: Yan Sun, University of Colorado Boulder.

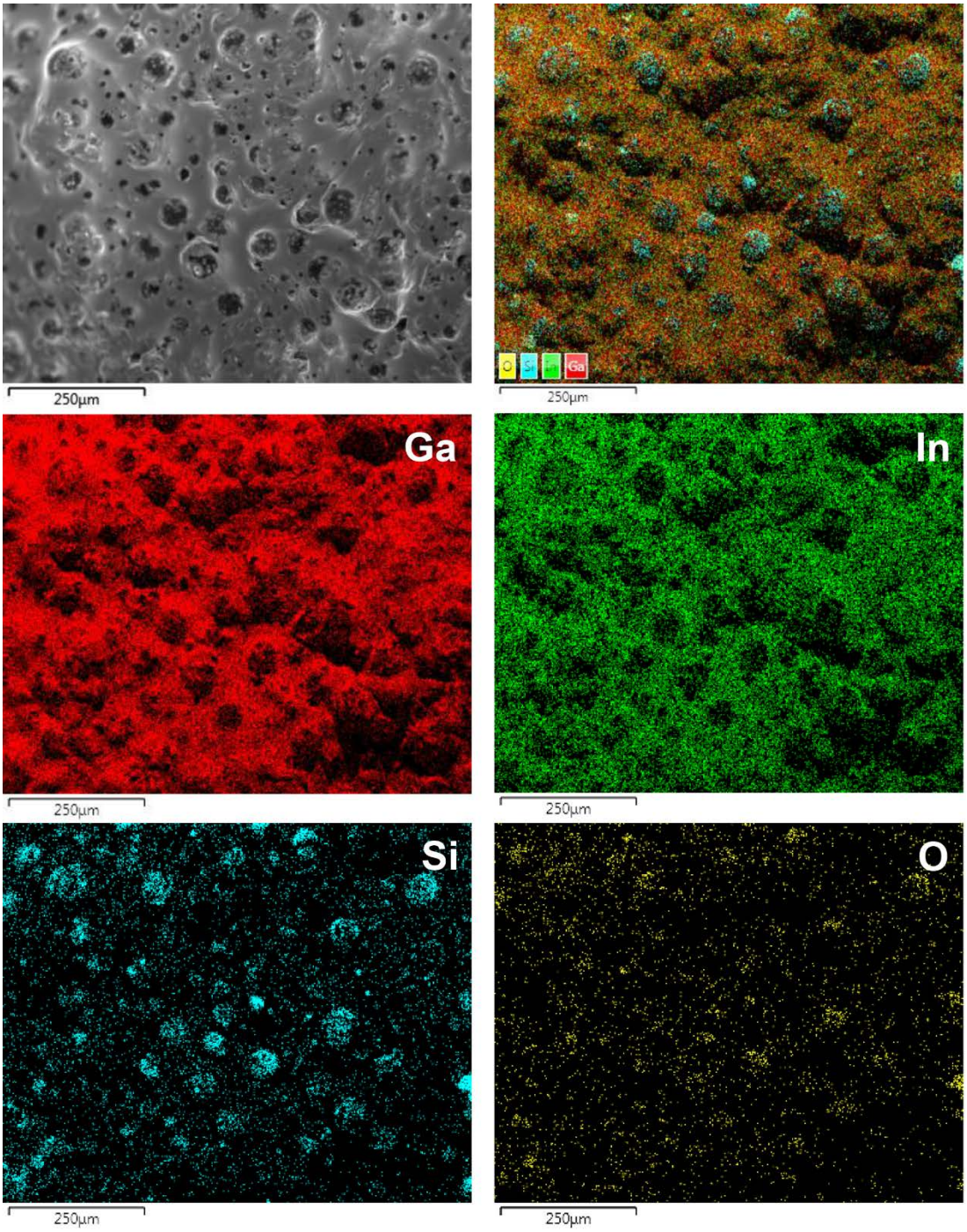

Fig. S4. Scanning electron microscope (SEM) image and energy spectrum mapping of liquid metal mixed with 0.35 wt.% SiO_2 microspheres (radius 40 μm).

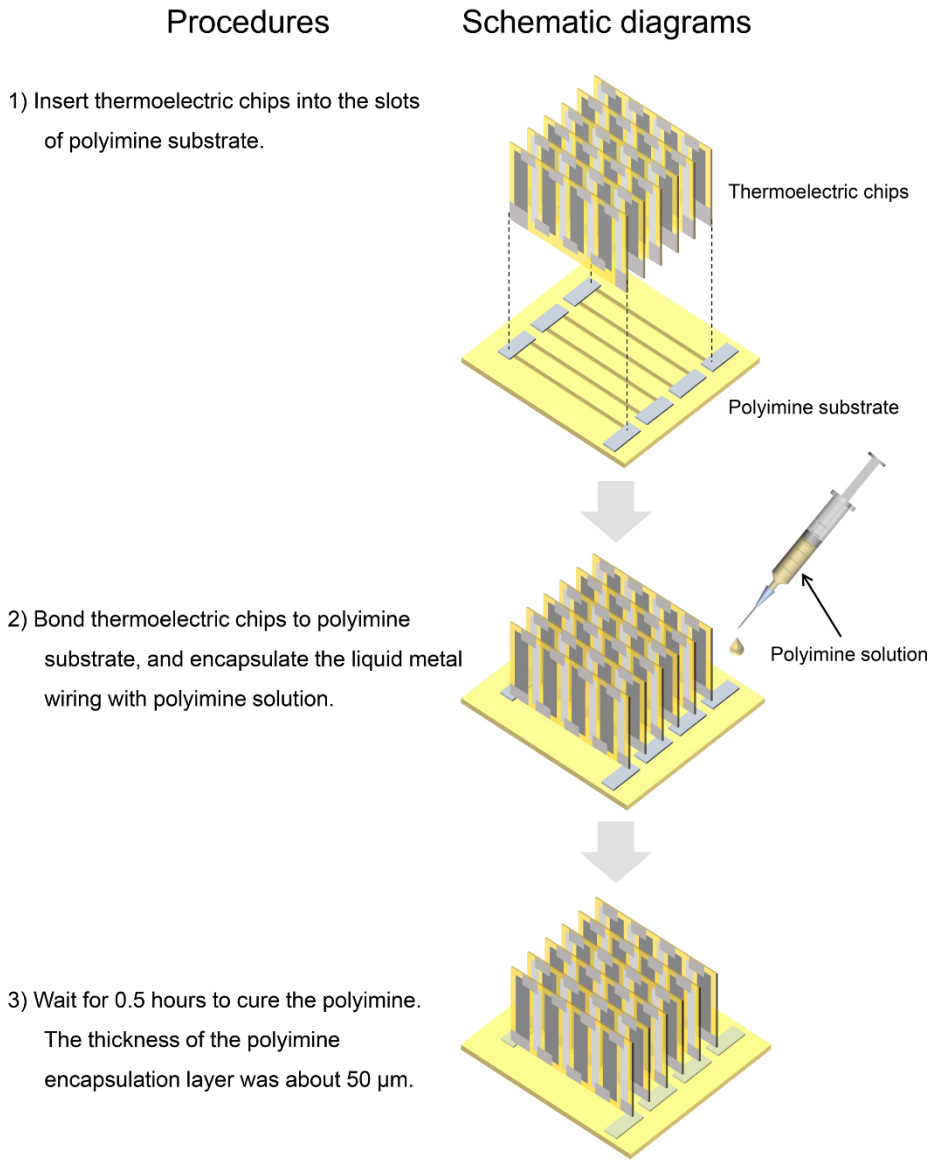

Fig. S5. Schematic illustration of step-by-step fabrication processes of thermoelectric generators.

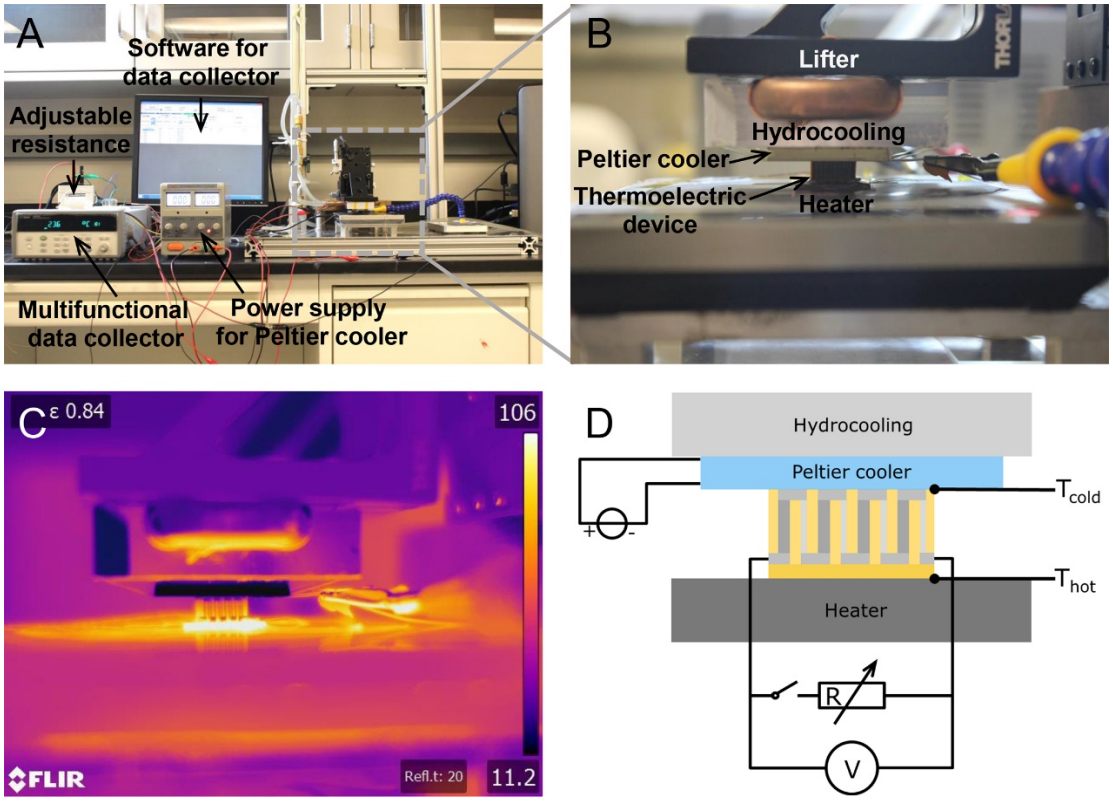

Fig. S6. Testing platform for the output of TEGs. (**A**) Overall testing setup. (**B**) A closer view of the cross section. The two-stage coolers can accurately control the cold side temperature of the TEG from 0 °C to room temperature. (**C**) Infrared image of (B). (**D**) Schematic of the testing setup. Photo credit: Yan Sun, University of Colorado Boulder.

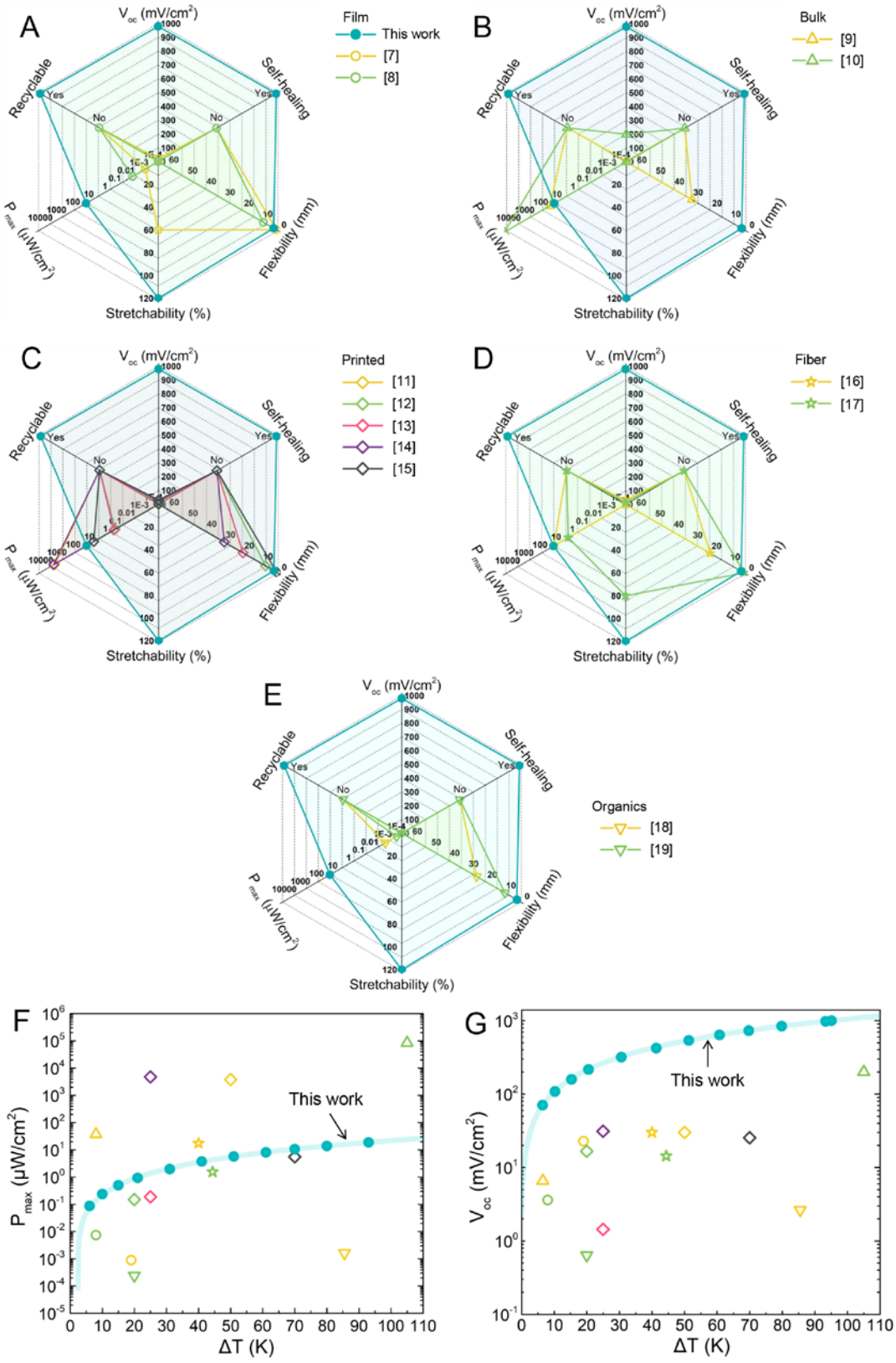

Fig. S7. Performance comparison between the TEG in this work and other flexible TEGs reported in the literature. (**A**) Film. (**B**) Bulk. (**C**) Printed. (**D**) Fiber. (**E**) Organics. Temperature difference (ΔT) dependent (**F**) max power densities P_{max} and (**G**) open-circuit voltage per unit area V_{oc}. The solid lines in (F) and (G) are the parabolic and linear fitting curves for measurement data, respectively.

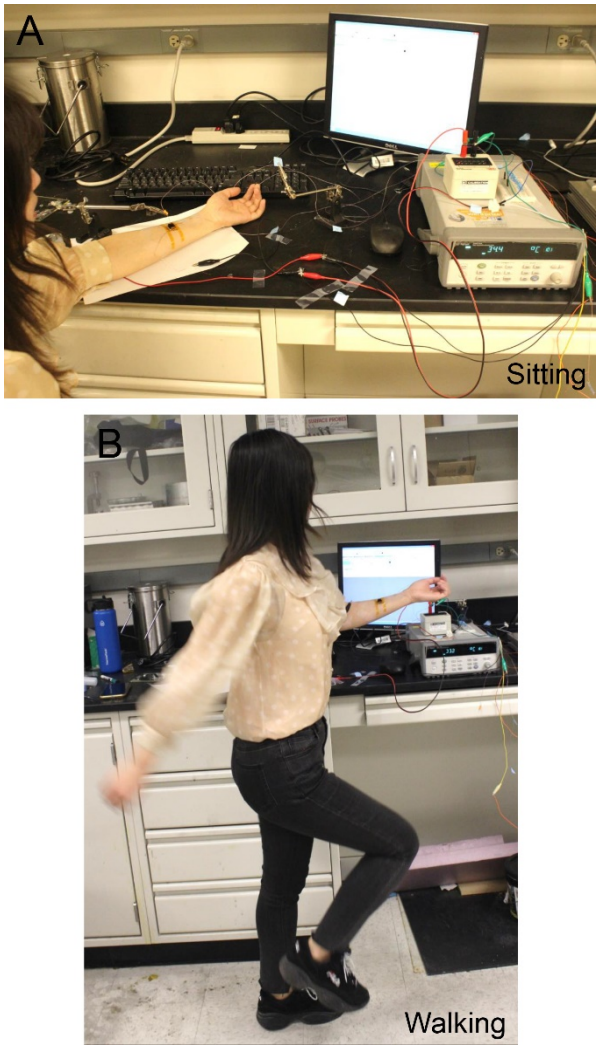

Fig. S8. Images of on-arm performance testing of a TEG during (**A**) sitting and (**B**) walking. Photo credit: Yan Sun, University of Colorado Boulder.

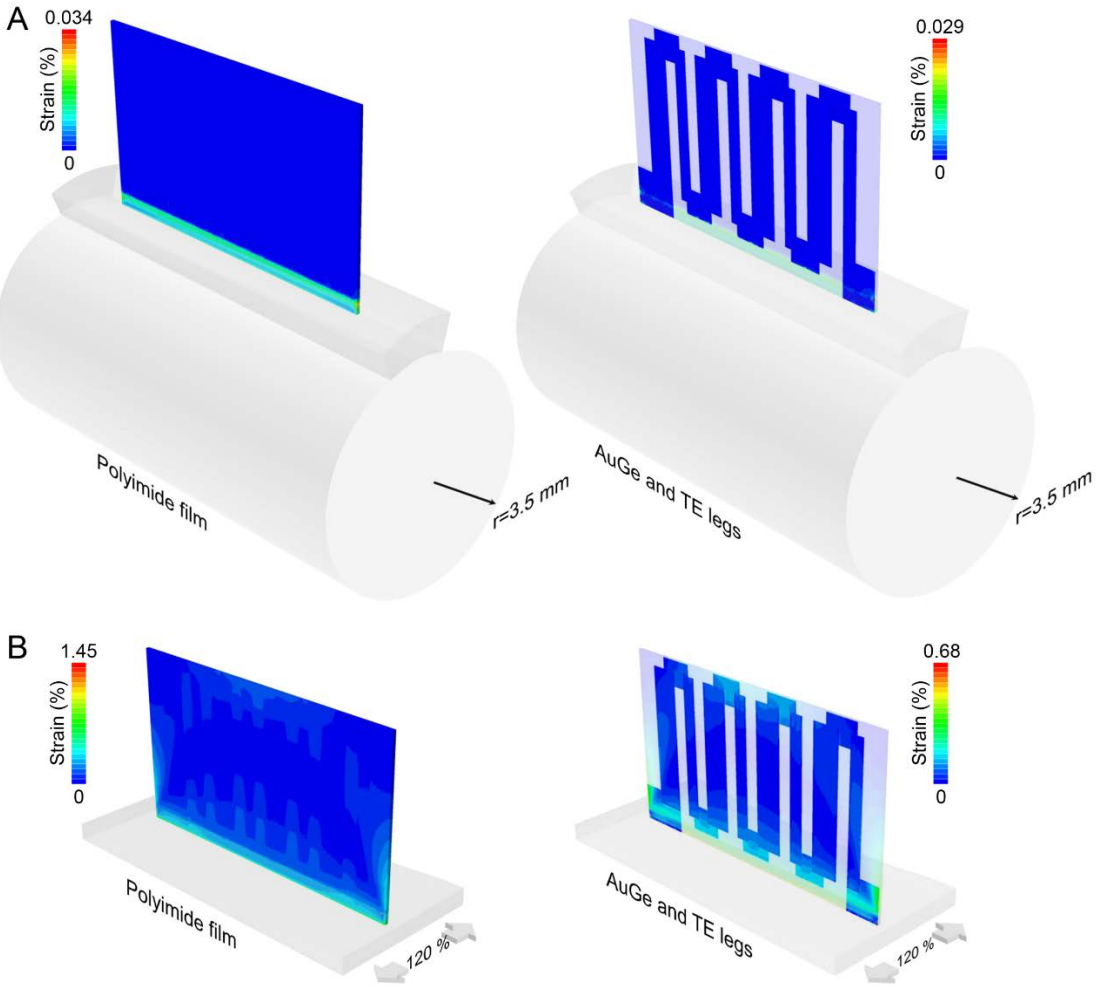

Fig. S9. Simulated strain distribution contours in the polyimide film, AuGe, and thermoelectric (TE) legs when a TEG is (**A**) bent at a radius of 3.5 mm and (**B**) stretched by 120%. All strains are below the failure limits of the corresponding materials.

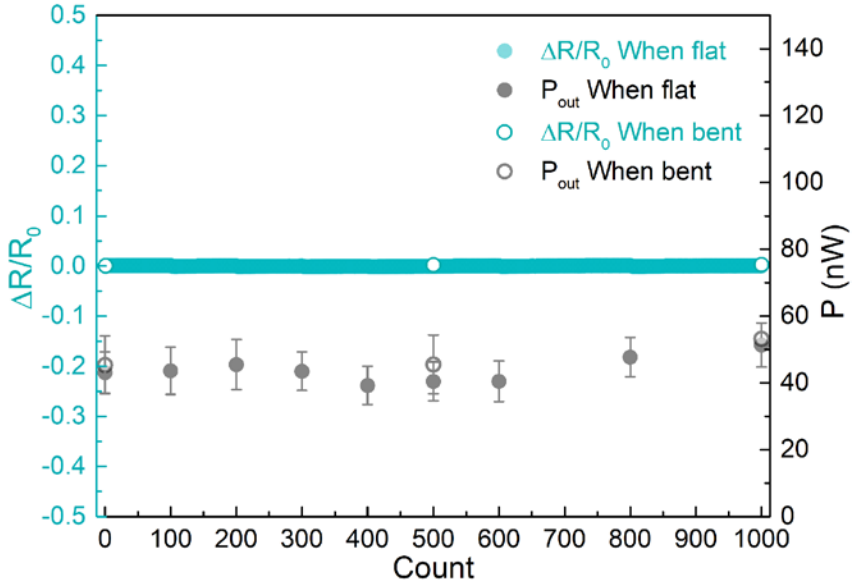

Fig. S10. Relative electrical resistance change ($\Delta R/R_0$) and power generation (P) stability over 1000 bending cycles with bending radius r =3.5 mm when the TEG is flat and bent. For the output power (P_{out}) measurements, the hot side temperature was kept at 41 °C, the cold side was natural convection, and the room temperature was around 26 °C.

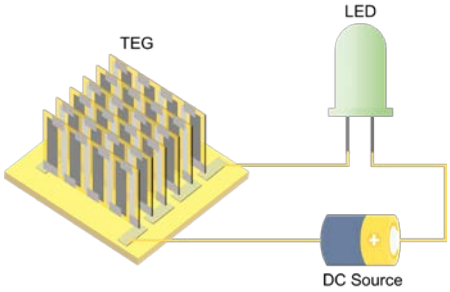

Fig. S11. Schematic illustration of the circuit to visually exhibit that the TEG is undamaged when stretched, cut, recycled, or reconfigured.

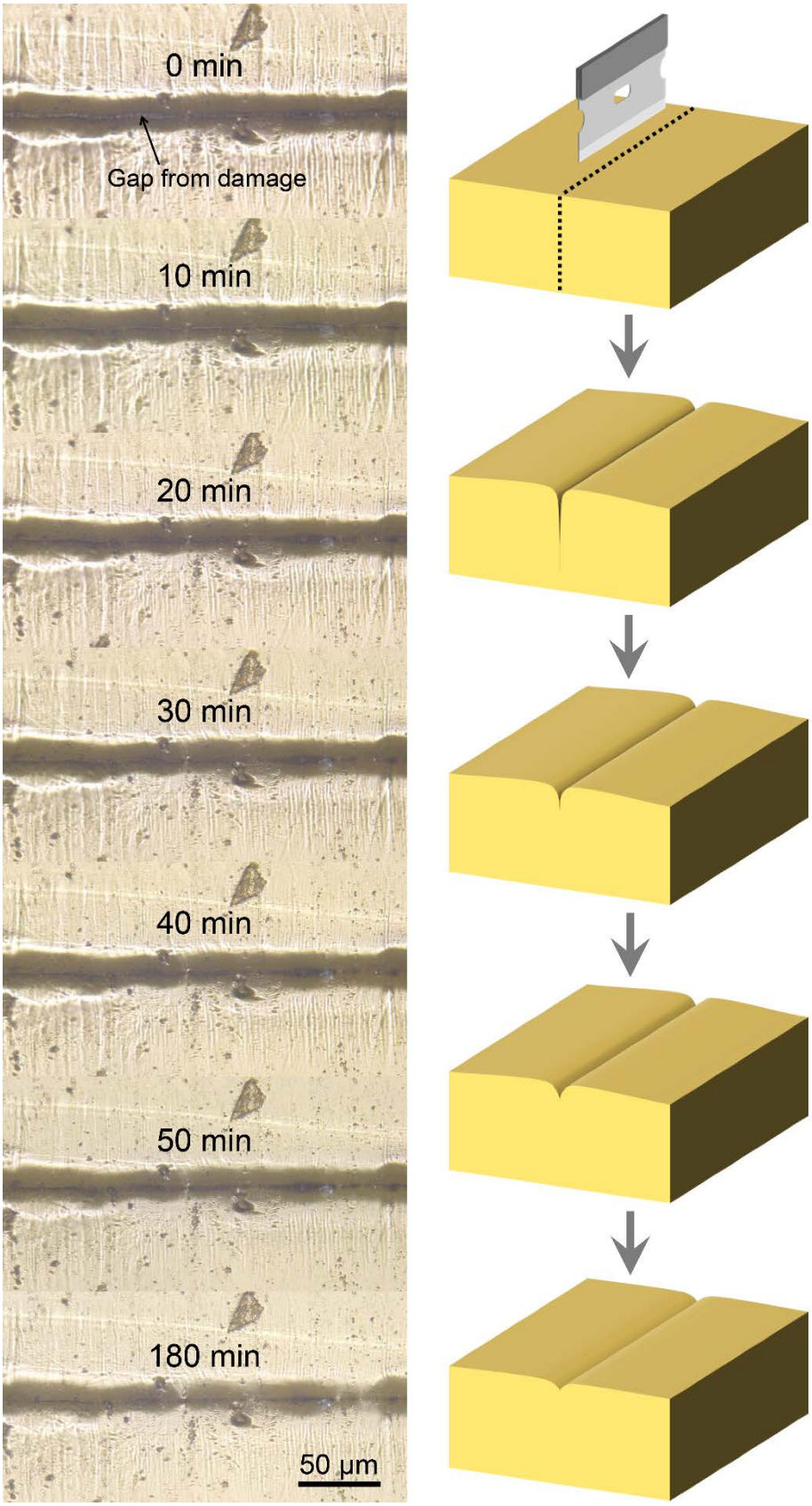

Fig. S12. Optical microscope images and schematic illustration of the self-healing process at room temperature.

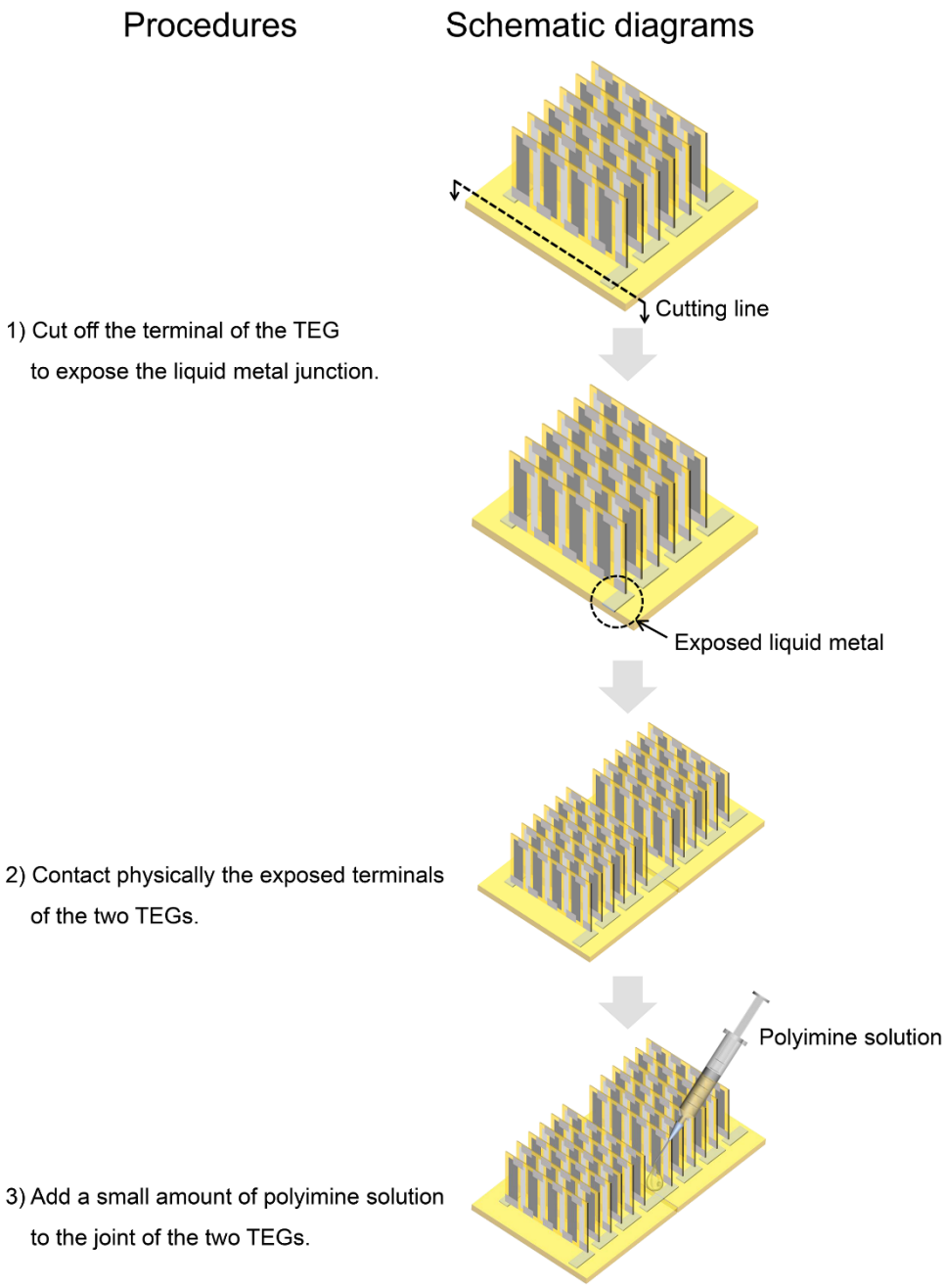

Fig. S13. Schematic illustration of step-by-step reconfiguration processes.

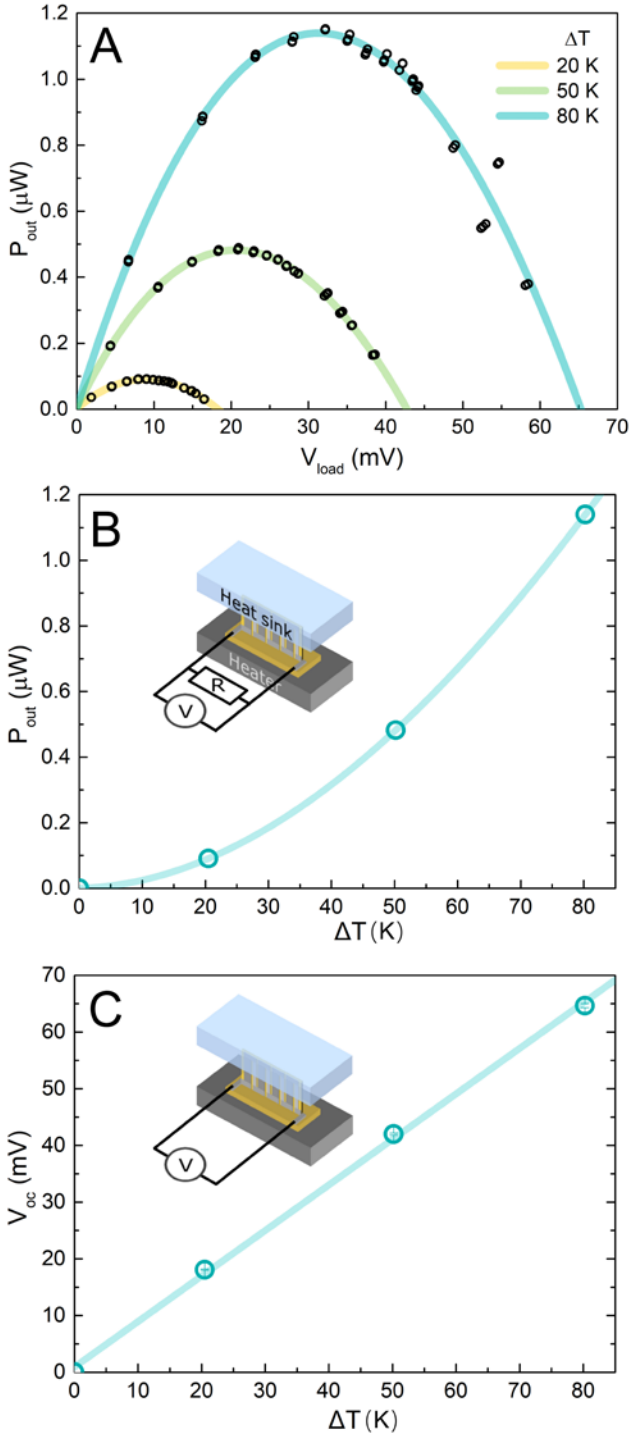

Fig. S14. Output performance of one thermoelectric chip. (**A**) Power generation (P_{out}) as a function of output voltage (V_{load}) at various temperature differences. The black points are measurement data. The cold side temperature (T_{cold}) was kept at 20 °C. (**B**) Maximum power generation at various temperature differences. (**C**) Open-circuit voltage (V_{oc}) at various temperature differences. The solid lines in (A) and (B) are fitting curves using parabolic functions. The solid line in (C) is a linear fitting curve.

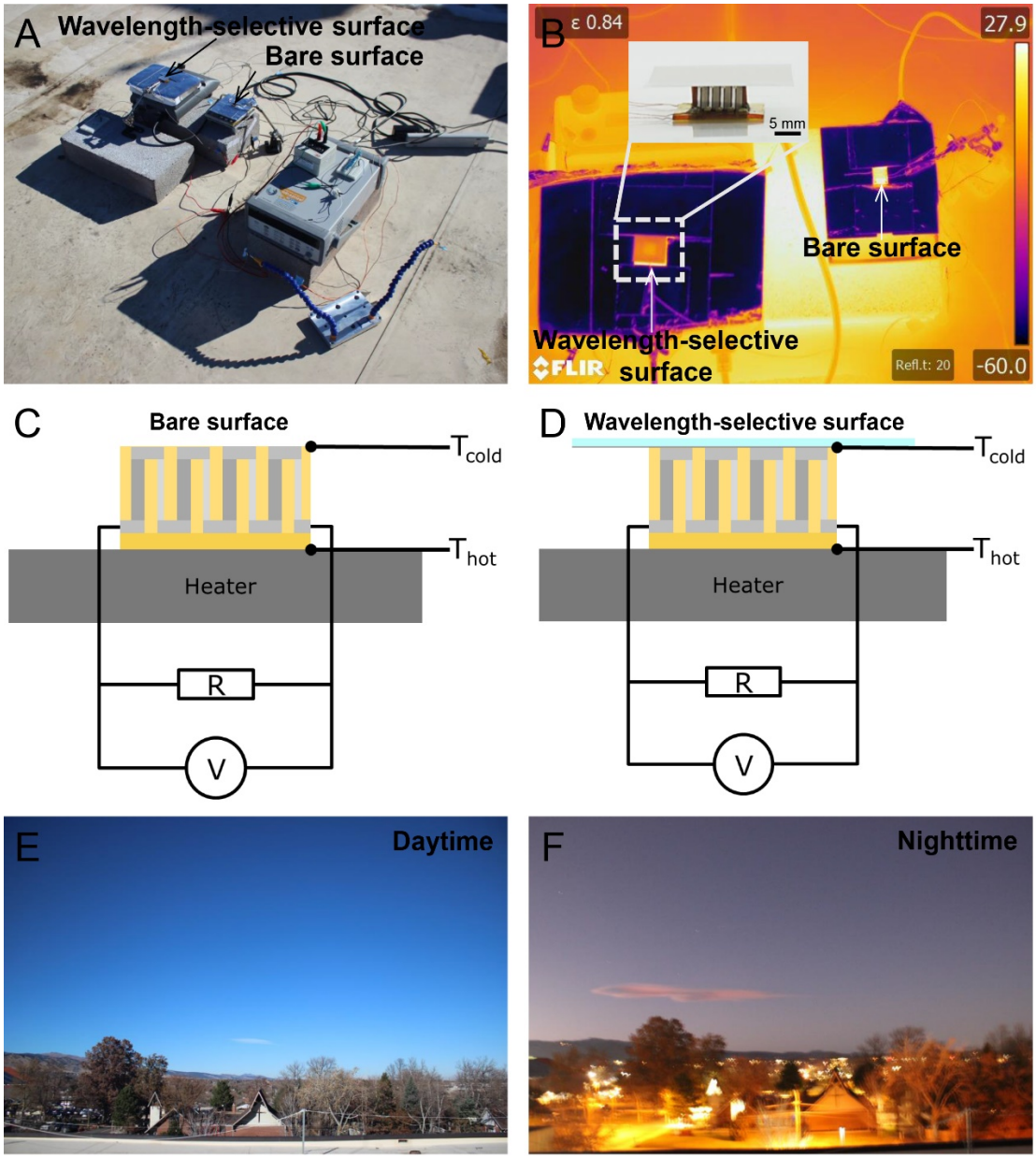

Fig. S15. Outdoor performance testing setup for TEGs. (**A**) Optical image of the entire testing setup. (**B**) Infrared image of the testing setup. The inset is an image of a TEG with a wavelength-selective surface. The wavelength-selective film was attached on the cold side of the TEG by using a pressure-sensitive tape. (**C, D**) Schematics of the testing setup. (**E, F**) Photos of sky conditions during the testing day. To simulate the human skin, we set the temperature of the heaters at 35 °C. Photo credit: Yan Sun, University of Colorado Boulder.

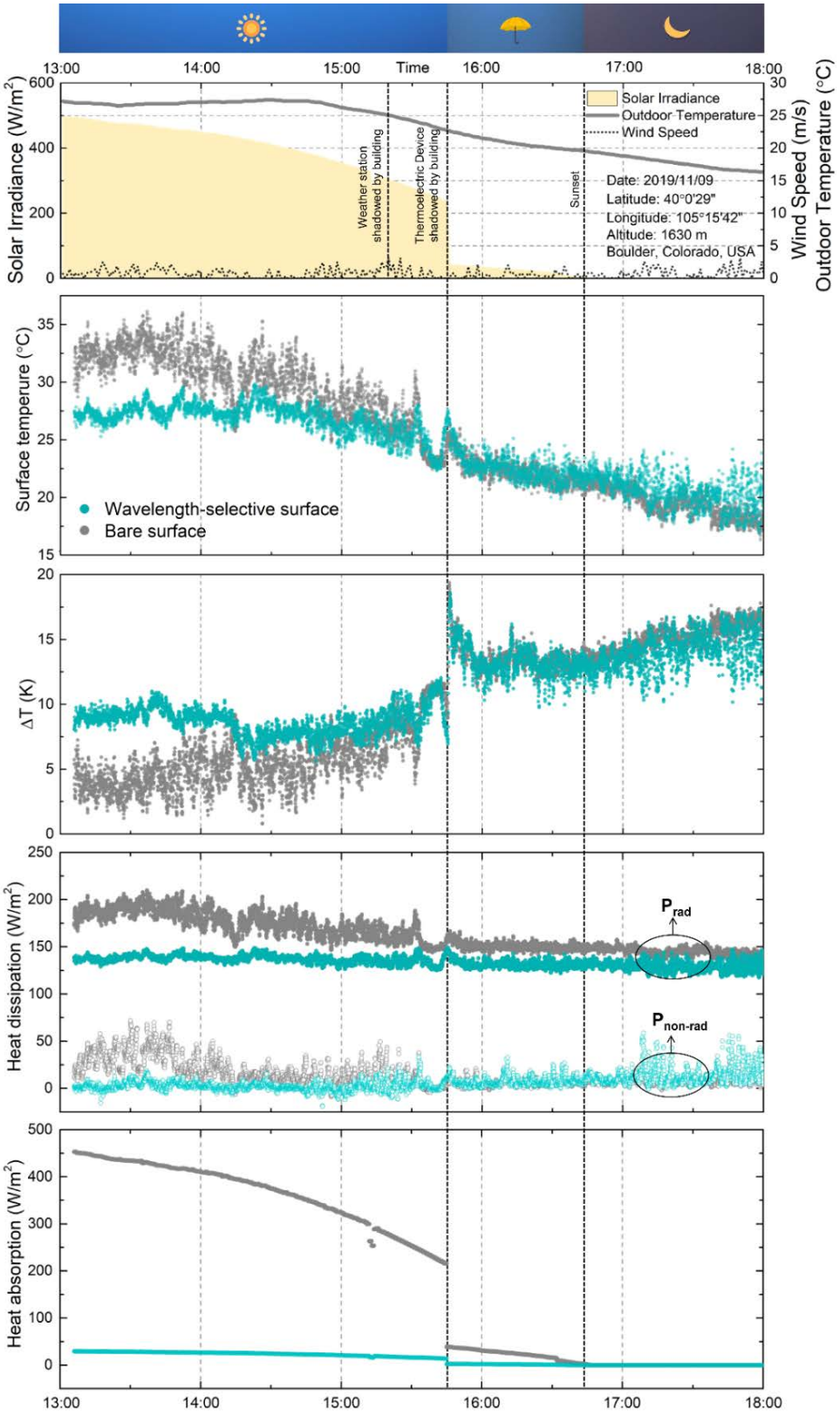

Fig. S16. Surface temperature (T_s), the temperature difference between the hot side and cold side of the TEGs (ΔT), calculated radiative (P_{rad}) and nonradiative ($P_{non\text{-}rad}$) heat dissipation and heat absorption. The solar irradiation between 15:18 and 15:45 is obtained by fitting the data between 13:00 and 15:18.

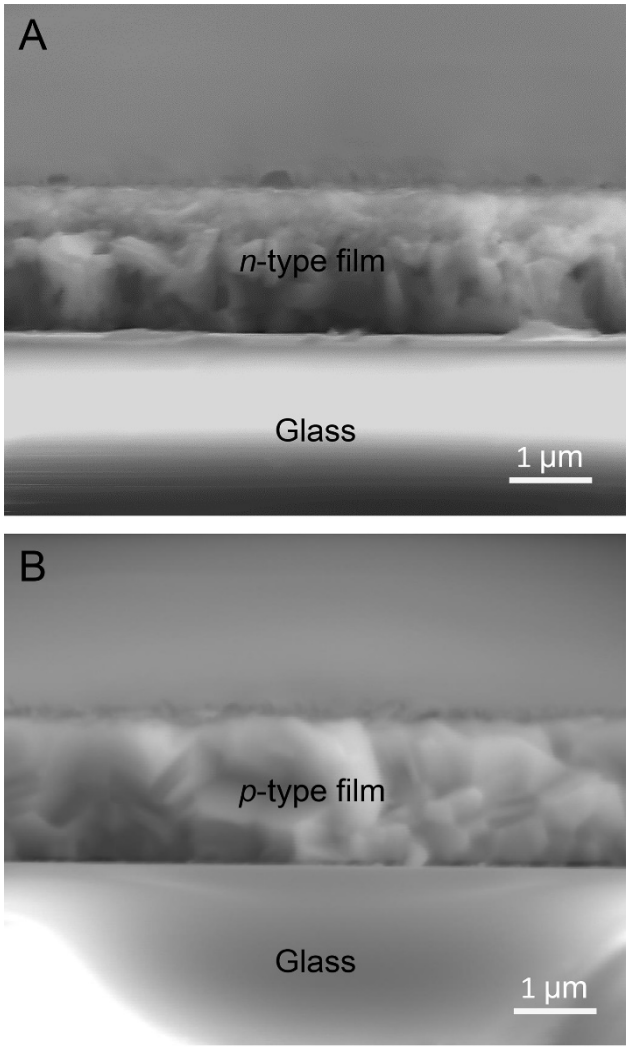

Fig. S17. SEM images of cross sections of (**A**) *n*-type and (**B**) *p*-type films. No grain orientations observed in both *n*-type and *p*-type films.

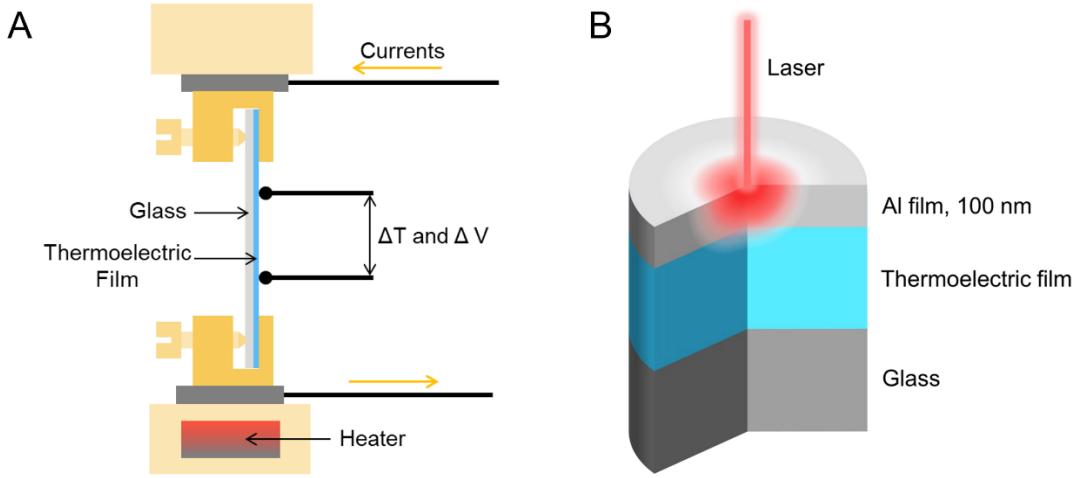

Fig. S18. Schematics of physical properties test methods for thermoelectric films. (**A**) Four probe method for Seebeck coefficient and electrical resistivity. (**B**) Time-domain thermoreflectance method (TDTR) for thermal conductivity.

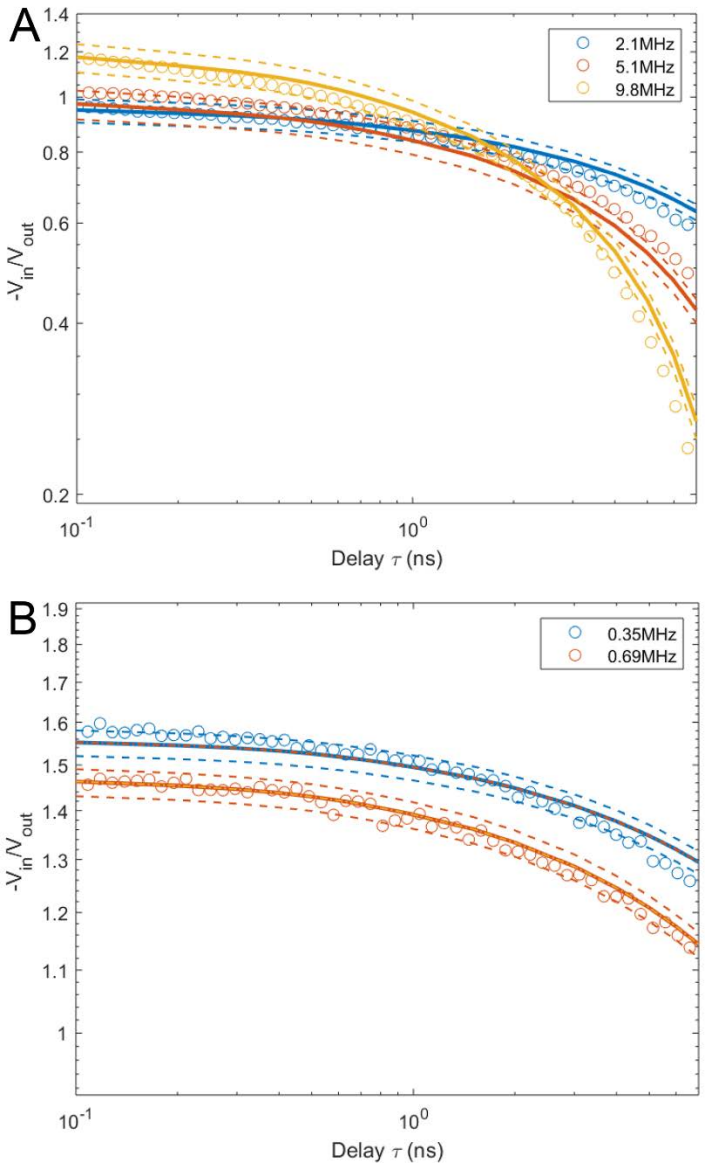

Fig. S19. Measured TDTR signal of (**A**) *n*-type and (**B**) *p*-type thermoelectric films with a spot radius of 7.5 μm using a 100 nm Al transducer and several modulation frequencies. The solid lines are fitting lines from a thermal model, and the dashed lines are 10% for *n*-type films, and 20% for *p*-type films bounds on the fitted through-plane thermal conductivity values. The best-fit thermal conductivity is listed in Table S1.

802 **Table S1.** The physical properties of thermoelectric films at room temperature.

Type	Composition (at.%)	Thickness (μm)	Resistivity (Ω•m)	Seebeck coefficient (μV/K)	Power Factor (μW/mK^2)	Thermal Conductivity (W/mK)	*ZT*
n-type	18.7Bi-75Te-6.3Se	1.6	3.66e-5	-145	584	1.315	0.13
p-type	36.7Sb-2.2Bi-61.1Te	1.75	1.06e-5	169	2694	1.285	0.63

803

Table S2. A summary of experimental results of flexible TEGs reported in the literature, grouped by fabrication methods of thermoelectric materials.

Type	Size, L×W×H (mm^3)	Number of Legs	ΔT (K)	P_{max} ($\mu W/cm^2$)	V_{oc} (mV/cm^2)	$P/N\Delta T^2$* ($10^{-3}\mu W/K^2$)	$V/N\Delta T^{\#}$ ($\mu V/K$)	Flexibility (mm)	Stretchability	Ref.
Film	12×12×7	112	93	18.625	980.043	5.15	271	3.5	120%	This work
	15×15×1	128	19	8.9E-4	22.8	0.0016	42.2	2†	60%	[7]
	45×30×2.1	760	8	7.4E-3	3.6	0.033	16	9†	—	[8]
Bulk	50×50×6	142	8	37.5	6.6‡	1651	357.5	30	—	[9]
	50×50×1.16	500	105	84000	200	80000	190.5	150	—	[10]
Printed	15×20×0.5	16	50	3800	30	28500	225	20†	—	[11]
	25×6×0.6	24	20	0.149	16.7	0.93	104.4	8§†	—	[12]
	50×50×4	16	25	0.187	1.44	23.38	180	20§†	—	[13]
	40×40×0.8	144	25	4780	31.25	42489	277.8	30	—	[14]
	120×120×0.17	1985	70	5.5	25.4	11.4	52.7	2†	—	[15]
Fiber	80×4×10	120	40	17.425	30	23.23	40	20†	—	[16]
	15×20×7.84	30	44.4	1.547	14.33	6.97	64.6	2§†	80%	[17]
Organics	140×140×0.5§	162	85.5	1.63E-3	2.65	0.046	75	25§†	—	[18]
	50×25×—§	16	20	2.4E-4	0.64	0.019	50	10§†	—	[19]

* $P/N\Delta T^2$ represents the max power of a single couple per K^2, where P is the max power of the TEG, and N is the number of the thermoelectric coups.

$^{\#}$ $V/N\Delta T$ represents the open-circuit voltage of a single couple per K, where V is the open-circuit voltage of the TEG.

§ The size was estimated by the information in these papers.

‡ The value was tested at the temperature difference (ΔT) of about 6.5 K.

† There wasn't a cyclic bending test at this radius.